

Iron, Copper, and Zinc Isotopic Fractionation in Seafloor Basalts and Hydrothermal Sulfides

Zhigang Zeng^{1,2,3,4}, Xiaohui Li^{1,4}, Shuai Chen¹, Jeroen de Jong⁵, Nadine Mattielli⁵,
Christopher Pearce⁶, Berit Lehrmann⁶, Bramley J. Murton⁶, and Haiyan Qi^{1,4}

¹Seafloor Hydrothermal Activity Laboratory, CAS Key Laboratory of Marine Geology
and Environment, Institute of Oceanology, Chinese Academy of Sciences, Qingdao,
China, ²Laboratory for Marine Mineral Resources, Qingdao National Laboratory for
Marine Science and Technology, Qingdao, China, ³University of Chinese Academy of
Sciences, Beijing, China, ⁴Center for Ocean Mega-Science, Chinese Academy of
Sciences, Qingdao, China, ⁵Laboratoire G-Time, Département des Géosciences,
Environnement et Société, Université Libre de Bruxelles, Brussels, Belgium, ⁶National
Oceanography Centre, Southampton, UK

Corresponding author: Zhigang Zeng (zgzenq@qdio.ac.cn)

Abstract

Studies on the Fe, Cu, and Zn isotopic compositions of volcanic rocks and sulfides provide an important tool for understanding magmatic, hydrothermal, and alteration processes. In this study, the $\delta^{56}\text{Fe}$ and $\delta^{57}\text{Fe}$ values of the MORBs are higher than those of the seafloor hydrothermal fluids, while the reverse is true for the $\delta^{66}\text{Zn}$ and $\delta^{68}\text{Zn}$ values, suggesting that basalt-fluid interactions preferentially incorporate isotopically light Fe and heavy Zn into the fluid, resulting in the relative enrichment of the heavier Fe and lighter Zn isotopes in altered basaltic rocks. Most of the $\delta^{56}\text{Fe}$ values (-1.96 to $+0.11\text{‰}$) of the sulfide minerals are within the range of the vent fluids, but they are significantly lower than those of MORBs and back-arc basin basalts (BABBs), suggesting that the Fe in the sulfides was mainly derived from the fluids. However, the majority of the $\delta^{56}\text{Fe}$ and $\delta^{57}\text{Fe}$ values of chalcopyrite are larger than those of sphalerite and pyrite. This suggests that high-temperature sulfide minerals are enriched in ^{56}Fe and ^{57}Fe , whereas medium- and low-temperature sulfides are depleted in ^{56}Fe and ^{57}Fe . Moreover, the $\delta^{65}\text{Cu}$ (-0.88 to -0.16‰) and $\delta^{66}\text{Zn}$ (-0.39 to -0.03‰) values of the sulfide minerals are significantly lower than those of the MORBs, BABBs, and fluids, suggesting that ^{63}Cu and ^{64}Zn were preferentially removed from the fluids and incorporated into the chalcopyrite and sphalerite, respectively. Consequently, vent fluid injection and deposition can cause the heavier Cu and Zn isotopic compositions of hydrothermal plumes, seawater, and sediments.

1. Introduction

The stable isotopic systematics of iron, copper, and zinc (Fe-Cu-Zn) have been applied extensively as a tool for tracking fluid pathways and for fingerprinting sources of volcanic rocks and seafloor hydrothermal systems (e.g., John et al., 2008; Liu et al., 2015; Rouxel et al., 2004a, 2004b; Sharma et al., 2001; Zhu et al., 2000). The Fe isotopic systematics of mid-ocean ridge basalts (MORBs), ocean island basalts (OIBs), and back-arc basin basalts (BABBs) have demonstrated that MORBs and BABBs have homogeneous Fe isotopic compositions, while OIBs are isotopically heterogeneous (Schuessler et al., 2009; Teng et al., 2013; Weyer & Ionov, 2007; Williams & Bizimis, 2014). However, in the olivine crystals of Hawaiian basalts, evidence of significant Fe isotopic fractionation during magmatic differentiation has been observed on both the whole-rock and crystal scales (Teng et al., 2008, 2011). Fe isotopic compositions of the silicate minerals in peridotite and pyroxenite xenoliths in Hawaiian basalts were also analyzed to explore the use of Fe isotopes as a tracer of both peridotite and pyroxenite components in the source of oceanic basalts (Williams & Bizimis, 2014). Moreover, the Fe isotopic compositions of the altered oceanic basalts from ODP Site 801C in the Mariana Trench exhibit depleted light Fe isotopes relative to the fresh basalts, suggesting the preferential leaching of light Fe during alteration (Rouxel et al., 2003).

Various volcanic rock types, including MORBs, OIBs, island arc basalts, as well as subduction-related andesites and dacites, have been systematically analyzed to investigate Cu isotopic fractionation during mantle metasomatism and partial melting and to characterize the Cu isotopic compositions of distinct silicate reservoirs in the Earth (Ben Othman et al., 2006; Herzog et al., 2009; Li et al., 2009; Liu et al., 2015). However, the Cu and Zn isotopic compositions of altered oceanic crustal (AOC) rocks recovered from IODP Site 1256 on the East Pacific Rise (EPR) indicate that low-temperature hydrothermal alteration results in limited Cu and Zn isotopic fractionation in AOC, while significant Cu and Zn isotopic fractionation occurs during high-temperature hydrothermal alteration (Huang et al., 2016; Little et al., 2014; Vance et al., 2008). Moreover, high-precision Zn isotope data for MORBs and OIBs have revealed that MORBs exhibit homogeneous $\delta^{66}\text{Zn}$ values (+0.25‰ to +0.30‰; Ben Othman et al., 2006; Doucet et al., 2016; Wang et al., 2017), which were similar to those of OIBs (+0.31±0.09‰; Chen et al., 2013; Herzog et al., 2009; Wang et al., 2017). Ben Othman et al. (2006) also reported that MORBs from different ocean basins exhibit little variation from their average composition of $\delta^{66}\text{Zn} = +0.25\text{‰}$. Moreover, it was established that the $\delta^{66}\text{Zn}$ of four andesitic samples from Merapi volcano are homogeneous, with values between +0.23‰ and +0.25‰ (Toutain et al., 2008).

Thus far, the Fe isotopic compositions of seafloor hydrothermal sulfides have been determined for hydrothermal systems on mid-ocean ridges (MORs) (Bennett et al., 2009;

81 German et al., 2008; Rouxel et al., 2004a, 2008; Severmann et al., 2004; Sharma et al.,
82 2001). On the Juan de Fuca Ridge, the hydrothermal fluids venting into the overlying
83 water column provide a source of light Fe isotopes to the deep oceans and contribute to
84 the Fe isotope variations observed in seafloor sediments (N. C. Chu et al., 2006; Sharma
85 et al., 2001). The Fe isotopic composition of the plume particles in the Rainbow
86 hydrothermal field on the Azorean segment of the Mid-Atlantic Ridge (MAR) has
87 remained invariant over at least the past 16,000 years, implying that changing the Fe
88 isotopic composition of the seawater in the North Atlantic Ocean requires changes in the
89 relative fluxes of Fe to the ocean (Beard, Johnson, Von Damm, et al., 2003; Severmann et
90 al., 2004). However, in the Lucky Strike, the light Fe isotopic compositions (as low as
91 3.24‰) can be explained by equilibrium fractionation during sulfide precipitation in the
92 subsurface environment, which provides further evidence for abiotic fractionation of Fe
93 isotopes in hydrothermal systems (Rouxel et al., 2004a). A study of the $\delta^{56}\text{Fe}$ of the 5°S
94 hydrothermal fields on the MAR concluded that a stable, dissolved Fe fraction may have
95 an isotopic signature that is heavier than that of the original hydrothermal fluid, and this
96 could be used to trace hydrothermally sourced dissolved Fe throughout the deep-ocean
97 (Bennett et al., 2009). Furthermore, in the hydrothermal fields on the EPR between 9°N
98 and 10°N, the $\delta^{56}\text{Fe}$ values of the marcasite/pyrite of a single chimney are lower than
99 those of the chalcopyrite and fluids, suggesting that the Fe isotopes of the sulfides and
100 fluids are in disequilibrium, which can be explained by isotopic exchange during the

precipitation of pyrite or during the rapid formation of pyrite from FeS (Polyakov & Soultanov, 2010; Rouxel et al., 2008; Sharma et al., 2001).

The Cu isotopic compositions of MAR sulfides indicate that the subsurface precipitation of Cu-rich sulfides does not significantly control the $\delta^{65}\text{Cu}$ values of the hydrothermal chimneys, and the oxidation of primary Cu-sulfides may be the major cause of Cu isotopic fractionation in hydrothermal systems (up to 3‰) (Fernandez & Borrok, 2009; Markl et al., 2006; Rouxel et al., 2004b; Shields et al., 1965). However, the presence of mid-ocean ridge sulfides (MORSS) with heavy $\delta^{65}\text{Cu}$ values can be explained by processes occurring on the seafloor, such as the hydrothermal reworking of previously altered sulfides by high-temperature fluids, while sulfides with negative $\delta^{65}\text{Cu}$ values may have undergone extensive recrystallization (Mason et al., 2005; Rouxel et al., 2004b). Furthermore, the chalcopyrite from the sulfide chimneys at 21°N and 13°N on the EPR, at 86°W on the Galapagos Rift in the Pacific, and at the Broken Spur field at 29°N on the MAR, exhibit a larger variation in $\delta^{65}\text{Cu}$ values, from -4.81 to +11.47‰ (Zhu et al., 2000). The $\delta^{65}\text{Cu}$ variations of the MORSS can be explained using a two-stage model, which involves the preferential leaching of $\delta^{65}\text{Cu}$ during hydrothermal processes, and subsequent isotopic exchange between the crystallized Cu-sulfides and fluids (Markl et al., 2006; Mason et al., 2005; Zhu et al., 2000). The $\delta^{65}\text{Cu}$ variation in the seafloor hydrothermal vents in the back-arc basins (eastern Manus basin, North Fiji back-arc basin (NFB), and northeastern Lau basin) and island arc settings (Tonga Arc) in the western

Pacific (Kim et al., 2014) may be attributed to Cu isotope fractionation during the alteration and redox reactions associated with the maturation of venting sites near the surface (Kim et al., 2014; Pękala et al., 2011; Rouxel et al., 2004b).

The Zn isotopic compositions of vent fluids on MORs, as well as those of chimney sulfides, indicate that there are large variations in the $\delta^{66}\text{Zn}$ values of hydrothermal fluids, which has been interpreted to suggest that Zn sulfide precipitation is a primary factor causing the variations in the $\delta^{66}\text{Zn}$ values of fluids (Fernandez & Borrok, 2009; John et al., 2008; Mason et al., 2005). However, the Cu and Zn isotopic compositions of the hydrothermal fluids of the eastern Manus BAB indicate the systematic enrichment of heavy Cu ($\delta^{65}\text{Cu} = +0.3 \pm 0.2\text{‰}$) and Zn ($\delta^{66}\text{Zn} = -0.04$ to $+0.94\text{‰}$) isotopes, which has been interpreted to be the result of seafloor precipitation/redissolution processes, rather than the result of the evaporation/condensation of metal-rich magmatic fluids at a certain depth (Dekov & Rouxel, 2012).

In this study, Fe, Cu, and Zn isotope analyses were performed on MORs, BAB sulfides (BABS), and their host MORBs collected from the EPR near 13°N , the EPR between 1° and 2°S , the Edmond hydrothermal field (EHF) on the Central Indian Ridge (CIR), area A on the Southwest Indian Ridge (SWIR), and the Sonne 99 hydrothermal field (S99HF) in the NFB (Figure 1). The goals of this study were to determine the Fe-Cu-Zn isotopic characteristics of the MORBs, MORs, and BABS, to determine the sources of these metals, and to investigate the effects of the fluid-rock interactions and

mixing between the fluids and seawater on the Fe-Cu-Zn isotopic compositions of MORS and BABS.

2. Sampling and methods

2.1. Sample collection, Descriptions, and Processing

The studied MORS and BABS, which formed from both focused high-temperature (>300°C) fluid outflow through chimneys and from medium- (300 to 200 °C) to low-temperature (<200°C) fluids from mounds (Bowers et al., 1988; Gallant & Von Damm, 2006; Ishibashi, Grimaud, et al., 1994; Ishibashi, Wakita, et al., 1994; Koschinsky et al., 2002; Merlivat et al., 1987; Michard et al., 1984; Schmidt et al., 2007), as well as their host MORBs and BABBs, respectively (e.g., Kumagai et al., 2008; Zeng et al., 2010, 2014; Zeng, Ma, et al., 2015; Zeng, Niedermann, et al., 2015), were recovered from seafloor hydrothermal fields using a TV-grab sampler in 2005, 2007, 2008, 2009, and 2010 during the DY105-17, DY115-19, DY115-20, and DY115-21 cruises of the R/V Dayang Yihao, respectively (Zeng et al., 2014; Zeng, Ma, et al., 2015; Zeng, Niedermann, et al., 2015). The BABS samples from the S99HF in the NFB were collected in 1998, during the SO134 cruise of the R/V Sonne for the German HYFIFLUX II project. Moreover, in the NFB, the S99HF is located directly south of the triple junction point at 16°50'S and is hosted by basaltic rocks, the trace element compositions of which indicate

that the magma generation was influenced by two different sources: normal MORB and OIB related to enriched MORB (Eissen et al., 1994; Kim et al., 2006; Koschinsky et al., 2002; Nohara et al., 1994).

Tables S1 and S2 and Figure 1 present information regarding the sampling locations and depths and the mineral compositions of the MORS, BABS, and their host MORBs. The major minerals of the host MORBs included olivine and plagioclase, with minor clinopyroxene and orthopyroxene. The MORS and BABS mineral aggregate samples consisted of major pyrite \pm marcasite, chalcopyrite, sphalerite, anhydrite, barite, opal, minor galena, and amorphous silica (Table S2).

The fresh MORB chips were powdered (200 mesh in size) using an agate mortar for the Fe, Cu, and Zn isotopic analyses. All the MORS and BABS samples were crushed and sieved to obtain sulfide mineral aggregates between >1 mm and 1 cm in size. The MORS and BABS chips were crushed with an agate mortar and pestle and sieved to obtain sulfide mineral grains between 50 μ m and 2 mm in size, following which the sulfides and several gangue minerals were separated by ethanol elutriation (Zeng et al., 2014; Zeng, Ma, et al., 2015; Zeng, Niedermann, et al., 2015). As most of the samples were fine grained and intergrown, an integrated mechanical separation method (involving a high-frequency dielectric splitter, a magnetic separator, and an electromagnetic separator) was used to obtain a monomineralic sulfide as described in Zeng et al. (2014; Zeng, Ma, et al., 2015; Zeng, Niedermann, et al., 2015). Thereafter, the sulfide minerals

were carefully manually selected under a binocular microscope to avoid sulfates and oxides, and then, they were ultrasonically cleaned in ultrapure alcohol to remove any seawater influences (Zeng et al., 2014). Finally, all of the sulfide mineral samples were ground to a <63 μm powder using an agate mortar for the Fe, Cu, and Zn isotopic analyses.

2.2. Fe, Cu, and Zn Isotopic Analyses

The isotopic ratios of all of the MORB, MORS, and BABS samples were measured on either a Nu Plasma I (Zn in basalts) or a Nu Plasma II (Fe, Cu, and Zn in basalts and sulfides) multiple collector-inductively coupled plasma-mass spectrometer (MC-ICP-MS, Nu Instruments, Wrexham, UK) at the Université Libre de Bruxelles (ULB, Laboratoire G-Time), Brussels, Belgium. The dissolution; the Fe, Cu, and Zn purifications; and the isotopic analyses were conducted using the established procedure described by Petit et al. (2008) and Sossi et al. (2015), but slightly modified, as described by Debret et al. (2018). In brief, the powdered samples (approximately 5 mg for the sulfide minerals and 50 mg for the bulk rocks) were dissolved in closed screw-top Savillex Teflon beakers using a mixture of double-distilled concentrated HF, HNO₃, and HCl for a minimum of ~3 days at 125°C. After complete dissolution was achieved, 1 ml of 8N HCl + 0.001% H₂O₂ was added to the beaker, and the solution was heated to dryness at 80°C. This process was repeated two or three times to ensure that all the cations were converted into chloride

species. The final residues were dissolved in 1 ml of 8N HCl + 0.001% H₂O₂ in preparation for the ion exchange separation. The Fe, Cu, and Zn in the samples were separated from the sample matrix constituents (e.g., Ti, Cr, and Mg) using an anion exchange resin (Bio-Rad AG1-X8, 100 to 200 mesh) in an HCl medium. A second passage for the Cu and Zn was preferred to avoid any spectral or non-spectral interferences from the potential residual matrix elements during the isotopic analysis.

The Cu and Zn isotope ratios were measured using the doping method with the addition of a JMC Zn (Art. Nr 13835, lot Nr 0620611.10, 'Zn110') or Cu (Art. Nr 13867, lot Nr 13.0140203.10, 'Cu310') in-house standard solution, and the sample-standard bracketing technique (Petit et al., 2008). The isotopic determinations were carried out in the wet plasma mode for the Zn in the basalts, while the Cu in the basalts and sulfides and the Zn in the sulfides were analyzed under higher sensitivity dry plasma conditions using an ESL Apex-Q desolvator (Elemental Scientific, Omaha, Nebraska, USA). The solution concentrations for the measurements were 400 µg/L of Zn (wet plasma) and 100 µg/L of Zn or Cu (dry plasma) in 0.05 M HNO₃.

To monitor the accuracy of the analyses and to report the data, the SRM NIST 976 Cu and Lyon JMC 3-0749L Zn reference solutions and the IRMM 3702 Zn certified reference material were measured (Ponzevera et al., 2006). The Cu and Zn isotopic data are reported in standard δ notation in per-mil (‰) against international reference materials SRM NIST 976 and JMC 3-0749L, respectively: $\delta^{65}\text{Cu} =$

221 $[(^{65}\text{Cu}/^{63}\text{Cu})_{\text{sample}}/(^{65}\text{Cu}/^{63}\text{Cu})_{\text{NIST 976}} - 1] \times 1000$ and $\delta^i\text{Zn} =$
 222 $[(^i\text{Zn}/^{64}\text{Zn})_{\text{sample}}/(^i\text{Zn}/^{64}\text{Zn})_{\text{JMC 3-0749L}} - 1] \times 1000$, where i refers to 66 or 68. Repeated
 223 measurements of the in-house JMC Cu110 and Zn310 solutions yielded average values of
 224 $0.00 \pm 0.04\text{‰}$ (2SD) ($n = 30$) for $\delta^{65}\text{Cu}_{110}$ and $0.00 \pm 0.07\text{‰}$ (2SD) ($n = 31$) for $\delta^{66}\text{Zn}_{310}$.
 225 The Cu_{NIST} yielded $\delta^{65}\text{Cu}_{110} = -0.97 \pm 0.13\text{‰}$ (2SD) ($n = 27$), while the Zn_{Lyon} yielded
 226 $\delta^{66}\text{Zn}_{310} = -0.10 \pm 0.04\text{‰}$ (2SD) ($n = 3$). Furthermore, the IRMM 3702 yielded $\delta^{66}\text{Zn}_{310}$
 227 $= -0.41 \pm 0.07\text{‰}$ (2SD) ($n = 11$), which relative to the Zn Lyon gives $\delta^{66}\text{Zn}_{\text{Lyon}} = -0.31 \pm$
 228 0.07‰ (2SD) ($n = 11$). This is in excellent agreement with the results of, for example,
 229 Moeller et al. (2012) and Petit et al. (2008), who reported $\delta^{66}\text{Zn}_{\text{Lyon}} = -0.29 \pm 0.05\text{‰}$
 230 (2SD) ($n = 5$) and $\delta^{66}\text{Zn}_{\text{Lyon}} = -0.32 \pm 0.04\text{‰}$ (2SD) ($n = 4$). The details of the analytical
 231 session conditions and the mass bias corrections have been described by Petit et al.
 232 (2008), and more recently, by Debret et al. (2018).

233 The Fe isotope analyses were carried out on a Nu Plasma II instrument in dry plasma
 234 and in medium resolution. A DSN-100 desolvator (Nu Instruments, Wrexham, UK) was
 235 used for the dry plasma conditions. The solution concentrations for the measurements
 236 were $800 \mu\text{g/L}$ of Fe and $1000 \mu\text{g/L}$ of Ni in 0.05 M HNO_3 . Two isotopic ratios were
 237 measured ($^{56}\text{Fe}/^{54}\text{Fe}$ and $^{57}\text{Fe}/^{54}\text{Fe}$) by applying the sample-standard bracketing method
 238 by means of IRMM 014 and external normalization and using Ni as a dopant. The data
 239 are reported in delta (δ) notation relative to the IRMM-014 standard (Taylor et al., 1992)
 240 and were calculated using the equation $\delta^i\text{Fe} = [(^i\text{Fe}/^{54}\text{Fe})_{\text{sample}}/(^i\text{Fe}/^{54}\text{Fe})_{\text{IRMM-014}} - 1] \times$

1000, where i refers to 56 or 57.

The accuracy and precision of the Fe isotope analyses were assured by analyzing reference material IRMM-014 as the bracketing standard and our in-house quality control standard 'MIX'. The mean Fe isotopic compositions of these standards were as follows. IRMM-014: $\delta^{56}\text{Fe} = 0.00 \pm 0.07\text{‰}$, and $\delta^{57}\text{Fe} = 0.01 \pm 0.09\text{‰}$ (2SD, $n = 68$). MIX: $\delta^{56}\text{Fe} = -1.55 \pm 0.11\text{‰}$, and $\delta^{57}\text{Fe} = -2.26 \pm 0.16\text{‰}$ (2SD, $n = 61$). The long-term averages (2014 to 2016) of the MIX standard are $\delta^{56}\text{Fe} = -1.55 \pm 0.10\text{‰}$, and $\delta^{57}\text{Fe} = -2.28 \pm 0.16\text{‰}$ (2SD, $n = 126$).

3. Results

3.1. Fe-Cu-Zn Isotopic Compositions of the MORBs

The Fe, Cu, and Zn isotopic data for the MORB samples are presented in Table 1. The MORBs on the EPR near 13°N, the EPR between 1° and 2°S, the CIR, and the SWIR exhibit $\delta^{56}\text{Fe}$ values between +0.06‰ and +0.18‰ (Table 1). The $\delta^{56}\text{Fe}$ values (+0.10 to +0.16‰, avg. +0.127‰, $n = 6$) of the basalt samples from the EPR near 13°N are similar to those from the EPR between 1° and 2°S (+0.06 to +0.18‰, avg. +0.129‰, $n = 7$) and the SWIR (+0.07 to +0.16‰, avg. +0.126‰, $n = 13$) (Table 1). Most of the $\delta^{56}\text{Fe}$ values of the MORBs (+0.06 to +0.18‰: this work) are within the range of previously studied OIBs (−0.11 to +0.18‰; Beard, Johnson, Skulan, et al., 2003; Teng et

al., 2013) but are slightly higher than those of previously studied MORBs (+0.07 to +0.14‰; Teng et al., 2013) (Figure 2).

The measured $\delta^{65}\text{Cu}$ values of the MORB samples vary from -0.10 to $+0.73$ ‰ (Table 1). With the exception of three basalt samples, which have $\delta^{65}\text{Cu}$ values (IR05-TVG10-1: -0.01 ± 0.03 ‰; IR05-TVG3-1: -0.04 ± 0.23 ‰; 20VII-S20-TVG17-1: -0.10 ± 0.08 ‰) were lower than those of previously studied MORBs (0 to +0.14‰; Liu et al., 2015; Savage et al., 2015), most of the $\delta^{65}\text{Cu}$ values of the remaining basalt samples are substantially higher than those of previously studied MORBs and OIBs (-0.07 to $+0.18$ ‰; Liu et al., 2015; Savage et al., 2015) (Figure 3).

The measured $\delta^{66}\text{Zn}$ and $\delta^{68}\text{Zn}$ values of the basalt samples vary from $+0.31$ to $+0.51$ ‰ and from $+0.62$ to $+1.06$ ‰ (Table 1), respectively, and are higher than those of previously studied MORBs ($\delta^{66}\text{Zn}$ of $+0.25$ to $+0.30$ ‰; $\delta^{68}\text{Zn}$ of $+0.53$ to $+0.60$ ‰; Ben Othman et al., 2006; Wang et al., 2017) and OIBs ($\delta^{66}\text{Zn}$ of $+0.25$ to $+0.40$ ‰; $\delta^{68}\text{Zn}$ of $+0.50$ to $+0.79$ ‰; Wang et al., 2017) (Figure 4). Furthermore, the $\delta^{66}\text{Zn}$ values of the MORB samples exhibit an increasing trend, from the EPR at 13°N to the EPR between 1° and 2°S to the CIR to the SWIR (Figure 4).

3.2. Fe-Cu-Zn Isotopic Compositions of the Sulfides

The Fe, Cu, and Zn isotopic data for the MORS and BABS samples are presented in Table 2. The measured $\delta^{56}\text{Fe}$ and $\delta^{57}\text{Fe}$ values of the sulfide samples range from -1.96 to

+0.11‰, and -2.89 to +0.19‰, respectively, with no evident relationship between $\delta^{56}\text{Fe}$, $\delta^{57}\text{Fe}$ and mineral type (pyrite, chalcopyrite, and sphalerite). The $\delta^{56}\text{Fe}$ values of the pyrite samples from the EPR near 13°N vary between -1.05‰ and -0.29‰ (avg. of -0.66‰, $n = 7$), which is within the range of the $\delta^{56}\text{Fe}$ values (-1.89 to -0.06‰) reported by Rouxel et al. (2008) for pyrite from the EPR between 9°N and 10°N. The $\delta^{56}\text{Fe}$ values of the pyrite from the MORS and BABS exhibit a larger range than those of the chalcopyrite (Figure 2). However, the $\delta^{56}\text{Fe}$ values of the pyrite samples from the EPR between 1° and 2°S range from -1.74 to -0.01‰ (avg. of -0.77‰, $n = 7$), while the majority of the $\delta^{56}\text{Fe}$ values (-0.18 to +0.11‰) of the chalcopyrite are substantially higher than those of the pyrite (Table 2). In the S99HF on the NFB, the $\delta^{56}\text{Fe}$ value of the chalcopyrite ($-0.18 \pm 0.05\text{‰}$) is also substantially higher than those of the pyrite and sphalerite samples (pyrite: $\delta^{56}\text{Fe}$ of -1.25 to -0.48‰, avg. of -0.91‰, $n = 3$; sphalerite: $\delta^{56}\text{Fe}$ of -1.17 to -0.90‰, avg. of -1.02‰, $n = 4$) (Table 2), which places it within the $\delta^{56}\text{Fe}$ range of the chalcopyrite from the EPR between 9°N and 10°N (-0.33 to -0.11‰; Rouxel et al., 2008). Furthermore, most of the $\delta^{56}\text{Fe}$ values of the MORS and BABS samples are significantly lower than those of the host MORBs (+0.06 to +0.18‰; Teng et al., 2013; this work) and BABBs (+0.087 to +0.106‰; Teng et al., 2013) (Figure 2) but are similar to those of the hydrothermal fluids (-1.85 to -0.14‰; $n = 49$; Moeller et al., 2014; Rouxel et al., 2008; Severmann et al., 2004; Sharma et al., 2001).

The measured $\delta^{65}\text{Cu}$ values of the chalcopyrite vary from -0.88 to -0.16‰. This

range is smaller than those of the $\delta^{56}\text{Fe}$ and $\delta^{57}\text{Fe}$ values of the MORs and BABS minerals (Table 2) and is lower than those of the host MORBs ($\delta^{65}\text{Cu}$ values of -0.10 to $+0.73\text{‰}$; Liu et al., 2015; Savage et al., 2015; this work) and the hydrothermal fluids ($\delta^{65}\text{Cu}$ values of $+0.1$ to $+0.5\text{‰}$; Dekov & Rouxel, 2012) (Figure 3).

The $\delta^{66}\text{Zn}$ and $\delta^{68}\text{Zn}$ values of the sphalerite range from -0.39 to -0.03‰ and from -0.77 to -0.03‰ (Table 2), respectively, which is significantly lower than those of the host MORBs ($\delta^{66}\text{Zn}$ of $+0.25$ to $+0.51\text{‰}$; Ben Othman et al., 2006; Wang et al., 2017; this work) and the hydrothermal fluids ($\delta^{66}\text{Zn}$ of 0.00‰ to $+1.33\text{‰}$; John et al., 2008) but is mostly within the range of seawater ($\delta^{66}\text{Zn}$ of -0.33 to $+0.96\text{‰}$; Little et al., 2014; Samanta et al., 2017; Zhao et al., 2014) (Figure 4).

4. Discussion

4.1. Fe-Cu-Zn Isotope Variations in the MORBs

4.1.1 Fe Isotopes

In this study, the $\delta^{56}\text{Fe}$ values of the MORBs exhibit a narrow range of Fe isotopic compositions ($\delta^{56}\text{Fe}$ of $+0.06$ to $+0.18\text{‰}$, avg. of $+0.13 \pm 0.05\text{‰}$, $n = 28$). However, the $\delta^{56}\text{Fe}$ range of the MORBs is slightly larger than that of previously studied MORBs ($+0.04$ to $+0.14\text{‰}$; Teng et al., 2013; Weyer & Ionov, 2007) (Figure 2), indicating that slight Fe isotopic fractionation occurred during the melting of the MOR mantle (Teng et

al., 2013; Weyer & Ionov, 2007). Moreover, the $\delta^{56}\text{Fe}$ and $\delta^{57}\text{Fe}$ values of the MORBs are higher than those of the hydrothermal fluids ($\delta^{56}\text{Fe}$ of -0.18 to -1.84‰ , $\delta^{57}\text{Fe}$ of -0.20 to -2.71‰ ; Moeller et al., 2014; Rouxel et al., 2008; Severmann et al., 2004; Sharma et al., 2001) (Figure 2). This suggests that during the hydrothermal fluid-basalt interactions, isotopically light Fe may be preferentially incorporated into the hydrothermal fluids, while the isotopically heavy Fe remains in the altered basaltic rocks (Rouxel et al., 2003).

However, several processes and factors that cause variations in the $\delta^{56}\text{Fe}$ values of volcanic rocks should be considered, including the following four factors: alteration and/or wall rock assimilation, degree of partial melting, fractional crystallization, and spreading rate (Anbar et al., 2005; Croal et al., 2004; Dauphas & Rouxel, 2006; Hibbert et al., 2012; Rouxel et al., 2003; Schuessler et al., 2009; Teng et al., 2008; Weyer et al., 2005; Weyer & Ionov, 2007; Weyer & Seitz, 2012; Williams et al., 2009; X. Zhao et al., 2012).

1) The studied basalt samples were fresh and unaltered, which is supported by their measured loss on ignition values (0.20% to 0.58%) (Table S4; Doucet et al., 2016) and previous studies of radiogenic isotopes (Kumagai et al., 2008; Zeng et al., 2010, 2014; Zeng, Ma, et al., 2015; Zeng, Niedermann, et al., 2015). Therefore, the influences of the alteration, wall-rock assimilation and biotic redox processes on the Fe isotopic compositions can be ruled out for the MORBs analyzed in this study.

2) The degree of Fe isotopic fractionation during partial melting is dependent on the

degree of partial melting (e.g., the TiO_2 content), the $\text{Fe}^{3+}/\Sigma\text{Fe}$ ($\Sigma\text{Fe} = \text{Fe}^{3+} + \text{Fe}^{2+}$) of the magma source, and the type of melting (buffered versus non-buffered) (Dauphas et al., 2009; Woodhead et al., 1998; Woodhead & Johnson, 1993). However, the variation in their TiO_2 contents is relatively small (1.19 to 1.93 wt.%) (Table S4), and there is no obvious relationship between the $\delta^{56}\text{Fe}$ values and TiO_2 contents of the different samples (Figure S1). Although the estimated $\text{Fe}^{3+}/\Sigma\text{Fe}$ ratios of the basalts vary from 0.15 to 0.35, this amount is still considered to be relatively small (Teng et al., 2013; Weyer & Ionov, 2007). Moreover, the range of the degree of partial melting of mantle materials during MORB production varies from 5 to 20% (Bézos & Humler, 2005; Christie et al., 1986; Frost & McCammon, 2008; Klein & Langmuir, 1987; Workman & Hart, 2005), which alone cannot produce a $\delta^{56}\text{Fe}$ isotopic variation of more than 0.02‰ (Dauphas et al., 2009; Poitrasson & Freydier, 2005; Schoenberg & von Blanckenburg, 2006; Teng et al., 2008). Thus, partial melting of the mantle cannot fully account for the 0.12‰ variation in the $\delta^{56}\text{Fe}$ values of the basalts analyzed in this study.

3) The $\delta^{56}\text{Fe}$ value may increase with the evolution of the magma fractional crystallization (as the SiO_2 content increases) (Heimann et al., 2008; Poitrasson & Freydier, 2005; Schuessler et al., 2009). Petrographic and geochemical studies have demonstrated that olivine and plagioclase are the major fractioning phases in our studied basalt samples. The removal of plagioclase should not affect the melt's Fe isotopic composition since it has a substantially lower FeO content than the residual melt (Teng et

al., 2013). Previous studies have suggested that olivine tends to have a light Fe isotopic composition relative to melts (Dauphas et al., 2009; Teng et al., 2008, 2011), and the crystallization of olivine can lead to an increase in the $\delta^{56}\text{Fe}$ value of the residual melt. However, the olivine contents (a major crystallization phase) of the studied basalt samples are similar, and there is no relationship between their $\delta^{56}\text{Fe}$ values and SiO_2 contents (Figure S1), indicating that different amounts of fractional crystallization of olivine and plagioclase cannot explain the variation in the $\delta^{56}\text{Fe}$ values of the studied basalts (Dauphas et al., 2009; Schuessler et al., 2009; Teng et al., 2008).

4) The spreading rate is a potential factor affecting magmatism at MORs. The 13°N EPR is a fast-spreading center, with a full spreading rate of 104 mm/year (Bluth & Ohmoto, 1988). The region between 1°S and 2°S in the EPR is an ultrafast spreading ridge segment, with a spreading rate of approximately 150 mm/year (Searle, 1983). The spreading center of the CIR has an intermediate-spreading rate in the EHF (approximately 48 mm/year; Van Dover et al., 2001). The SWIR is an ultraslow-spreading ridge, with a spreading rate of approximately 14 mm/year (DeMets et al., 1994; Patriat and Segoufin, 1988). These ridges and ridge segments constitute the end-members of the global MOR spectrum, providing natural laboratories for testing the potential control exerted by the spreading rate on mantle melting. However, no clear relationship has been found between the variations in the Fe isotopic compositions of basalts from different ridge segments and the local spreading rates of the ridge segments

(Figures 5a, S2), suggesting that the variation in spreading rate did not significantly affect the Fe isotopic compositions of the basalts.

As previously discussed, the seafloor alteration, partial melting, fractional crystallization, wall-rock assimilation, and MOR spreading rate are insufficient to explain the slight variation in the Fe isotopic composition. Moreover, distinct mantle source regions have previously been invoked to explain the elemental (Dasgupta et al., 2010; Prytulak & Elliott, 2007) and radiogenic isotopic (Hofmann, 1997; Salters et al., 2011; Stracke et al., 2005; Workman et al., 2004) signatures of many oceanic basalt suites. This suggests that the clear variation in the Fe isotopic compositions of the basalts in this study supports the concept of Fe isotopic heterogeneity in the Earth's lithospheric mantle (Rouxel et al., 2003; Teng et al., 2013; Williams & Bizimis, 2014). However, the MOR magma source's Fe isotopic heterogeneity and the different mantle melting processes require further investigation.

4.1.2 Cu Isotopes

The Cu isotopic compositions of the MORB samples exhibit significantly greater variations (−0.10 to +0.73‰, Table 1) than those of previously studied MORBs (0 to +0.14‰; Liu et al., 2015; Savage et al., 2015). These values are also slightly higher than those of previously studied OIBs (−0.07 to +0.18‰; Liu et al., 2015; Savage et al., 2015) (Figure 3), implying that during melting in the MOR, heavy ⁶⁵Cu was more likely to be

401 incorporated into the basaltic melt than into the ocean island environment.

402 The rather large range of the Cu isotopic compositions of the studied MORBs is
403 difficult to explain by high-temperature equilibrium Cu isotopic fractionation, such as by
404 partial melting of the mantle, which generates a limited amount Cu isotopic fractionation
405 and is distinct from the behavior of the Fe isotopes, which are significantly fractionated
406 during mantle partial melting (Liu et al., 2015; Weyer and Ionov, 2007). However, mantle
407 metasomatism can produce Cu isotopic fractionation (Fernandez & Borrok, 2009; Liu et
408 al., 2015). Metasomatism in basalts potentially results in sulfide dissolution/breakdown
409 or precipitation (Reisberg et al., 2005). If redox reactions are involved, the released Cu
410 may be isotopically heavy (Fernandez & Borrok, 2009), leaving the metasomatized
411 basalts isotopically lighter than primary MORBs. In contrast, the precipitation of
412 secondary minerals from fluids that have previously leached Cu from sulfides may enrich
413 the basalts in heavy Cu isotopes. During this process, isotopic fractionation may or may
414 not occur depending on which secondary phase is precipitated. Moreover, the patterns of
415 light rare earth elements (LREEs) and the lack of metasomatic minerals can be used to
416 evaluate the effects of metasomatism (Z. Y. Chu et al., 2009; Liu et al., 2015; X. Zhao et
417 al., 2015; Zheng et al., 2005). The metasomatized basalts exhibit LREE-enriched patterns
418 ($(\text{La}/\text{Sm})_N > 1$) and commonly contain metasomatic products (e.g., phlogopite), whereas
419 the non-metasomatized basalts display LREE-depleted or flat rare earth element patterns
420 and lack visible metasomatic minerals (Liu et al., 2015). Moreover, evidence of

metasomatism was not observed in most of the studied samples ($(\text{La}/\text{Sm})_{\text{N}} = 0.41\text{--}0.98$, avg. of 0.66, $n = 22$, except for samples 20III-S10-TVG7 and IR05-TVG4-1) (Figure S3); thus, the influence of metasomatism on the variation in the Cu isotopic compositions of the basalts can be ruled out. However, samples 20III-S10-TVG7 and IR05-TVG4-1, which have $(\text{La}/\text{Sm})_{\text{N}} > 1$ (1.21 and 1.01, respectively) and higher $\delta^{65}\text{Cu}$ values (0.55‰ and 0.69‰, respectively) than the other studied samples, can be explained by the influence of metasomatism via melt/fluid-rock interactions (Fernandez & Borrok, 2009; Liu et al., 2015).

Similar to the $\delta^{56}\text{Fe}$ variability, one explanation for the relatively large variation in the $\delta^{65}\text{Cu}$ values of the basalt samples is that they were derived from Earth's $\delta^{65}\text{Cu}$ -heterogeneous lithospheric mantle (Liu et al., 2015; Savage et al., 2014). This also implies that the varied Cu isotopic compositions of the studied MORBs may result from the $\delta^{65}\text{Cu}$ heterogeneity of their mantle sources.

4.1.3 Zn Isotopes

The Zn isotopic values of the studied MORB samples range from +0.31 to +0.51‰, which significantly exceeds the $\delta^{66}\text{Zn}$ range of previously reported MORBs (+0.26 to +0.30‰; Wang et al., 2017) and is higher on average than those of previously studied OIBs (+0.25 to +0.40‰; Ben Othman et al., 2006; Wang et al., 2017) (Figure 4). This implies that the magma evolution processes may have caused Zn isotopic fractionation,

and during melting in the MOR, heavy ^{66}Zn and ^{68}Zn were more likely to be incorporated into the basaltic melt than into the ocean island environment (Ben Othman et al., 2006; Wang et al., 2017).

However, the sedimentary carbonates exhibit substantially heavier Zn isotopic compositions (up to +1.34‰; Kunzmann et al., 2013; Pichat et al., 2003) compared to the studied MORBs (+0.31 to +0.51‰), and the recycling of sedimentary carbonates into the mantle may result in elevated $\delta^{66}\text{Zn}$ values, which has been observed in continental basalts from eastern China (Liu et al., 2016). Moreover, certain highly evolved silica-rich rocks (e.g., pegmatites) may exhibit high $\delta^{66}\text{Zn}$ values (+0.53 to +0.88‰; Telus et al., 2012), and mantle metasomatism processes may cause significant Zn isotopic variations in mantle rocks (Wang et al., 2017). Therefore, metasomatism by silica-rich melts may be responsible for the heavier $\delta^{66}\text{Zn}$ values of the basalts. However, the studied basalt samples recovered from the MOR tectonic setting with mafic/ultramafic magma were the major host magmas, and the addition of sedimentary carbonates and silica-rich rocks to the magma source is unlikely. Moreover, Zn is a monovalent element (Lodders, 2003); and thus, isotope fractionation induced by a change in the oxidation state can be excluded (Wang et al., 2017). Fractional crystallization of basaltic magmas and mantle partial melting are other possible mechanisms that could cause the Zn isotopic difference between the basalts and the mantle magma (Wang et al., 2017). Moreover, fractional crystallization has been proposed to explain the Zn isotopic variations observed in the

Kilauea Iki lavas (Chen et al., 2013). The isotopically heavier Zn basalts were thought to undergo fractionation of olivine and Fe–Ti oxides, whereas the basalts with the lightest $\delta^{66}\text{Zn}$ were interpreted to be the result of olivine and chromite accumulation (Chen et al., 2013). Furthermore, experimental studies have demonstrated that spinel is one of the major Zn hosts in basaltic magma (Davis et al., 2013; Le Roux et al., 2011), as it is isotopically heavier than other coexisting silicate minerals (Ol, Cpx, and Opx) (Wang et al., 2017). Therefore, the preferential melting of spinel is another likely mechanism for Zn isotopic fractionation, and the $\delta^{66}\text{Zn}$ of the residual melt became lighter when the spinel was exhausted. That is, the melts become isotopically heavier as larger amounts of spinel were incorporated into the melts, until complete melting of the spinel occurred. Thus, spinel melting is a reasonable mechanism for the Zn isotopic fractionation produced during partial melting of the mantle (Wang et al., 2017).

However, as previously discussed, olivine and plagioclase are the major fractionating phases, and the degrees of partial melting of the studied basalt samples are similar. Chen et al. (2013) found that fractional crystallization causes only very limited ($\leq 0.1\%$) Zn isotopic fractionation between lavas and their related cumulates. Therefore, it appears that fractional crystallization and/or the degree of partial melting of the mantle cannot explain the large variations in the Zn isotopic composition of our samples.

However, mantle heterogeneity has been suggested as a potential cause of Zn isotopic fractionation. This phenomenon has been used to explain the distinctly different

Zn isotopic compositions of fertile lherzolites and refractory spinel harzburgites (Chen et al., 2013; Doucet et al., 2016; Ionov et al., 2010). This suggests that Earth's heterogeneous lithospheric mantle may be a major cause of the distinct variation in the $\delta^{66}\text{Zn}$ values of our basalts.

It is interesting that the studied samples not only exhibit heterogeneous isotopic compositions, but there is a generally increasing trend in the $\delta^{66}\text{Zn}$ values of the MORBs from the EPR to the CIR to the SWIR (Figure 5c). This, coupled with the different MOR spreading rates, suggests that ^{66}Zn and ^{68}Zn are more likely to be incorporated into the basaltic magma under the ultra-slow-spreading SWIR than that under the fast-spreading EPR. Therefore, the variation in the MOR spreading rates can explain the variations in the Zn isotopic values of the different MOR tectonic settings. This implies that a faster spreading rate may result in lighter Zn isotopic values, i.e., closer to a MORB-like Zn isotopic composition.

4.2. Fe-Cu-Zn Isotopic Variations in the MORS and BABS

4.2.1 Fe Isotopes

It is well known that the hydrothermal activity on the EPR near 13°N, on the EPR between 1°S and 2°S, in the EHF on the CIR, and in area A on the SWIR, are hosted by MORBs, while that in S99HF on the NFB is hosted by BABBs (Zeng et al., 2010, 2014, 2017; Zeng, Ma, et al., 2015; Zeng, Niedermann, et al., 2015). The Fe isotopic

compositions of the hydrothermal fluids (-1.85 to -0.14‰ ; Moeller et al., 2014; Rouxel et al., 2008; Severmann et al., 2004; Sharma et al., 2001) (Figure 2) differ significantly from the Fe isotopic compositions ($+0.06$ to $+0.18\text{‰}$; Teng et al., 2013; this work) of the MORBs and BABBs, which are substantially lower than those of the host basalts ($+0.06$ to $+0.18\text{‰}$; Teng et al., 2013; this work). Therefore, the Fe isotopic compositions of sulfides can be used as evidence to determine the diagnostic isotopic signature of the Fe released into the oceans by seafloor hydrothermal vents and the interactions between the various Fe reservoirs (Severmann et al., 2004).

The $\delta^{56}\text{Fe}$ values of the MORS and BABS minerals range from -1.96 to $+0.11\text{‰}$ (Table 2), which are significantly lower than those of the host basalts ($+0.06$ to $+0.18\text{‰}$; Teng et al., 2013; this work) (Figure 2), and are generally similar to the $\delta^{56}\text{Fe}$ values of hydrothermal fluids (-1.85 to -0.14‰ ; Moeller et al., 2014; Rouxel et al., 2008; Severmann et al., 2004; Sharma et al., 2001) (Figure 2). This indicates that the hydrothermal fluids are a source of the Fe in the sulfide minerals, and the ^{54}Fe in their host MORBs and BABBs is more likely to be incorporated into the fluids during fluid-basalt interactions. Thus, it has been suggested that hydrothermal fluids also provide a source of light Fe isotopes to the deep oceans (Bennett et al., 2009; Moeller et al., 2014; Rouxel et al., 2008; Severmann et al., 2004; Sharma et al., 2001), and the interaction between the host basalt and the fluid results in preferential leaching of lighter Fe isotopes from hydrothermally altered basaltic rocks, while the heavier Fe isotopes remain behind

in the AOC (Bullen et al., 2001; Johnson et al., 2002, 2003; Polyakov & Mineev, 2000; Rouxel et al., 2003; Schauble et al., 2001; Sharma et al., 2001). This implies that a plate subduction component containing altered rocks (with heavier Fe isotopic compositions) has an influence on BAB and IA magma sources, thereby resulting in the preferential enrichment of heavier Fe isotopes in the BAB and IA volcanic rocks.

The chalcopyrite has a limited range of $\delta^{56}\text{Fe}$ values between -0.18‰ and $+0.11\text{‰}$, indicating a small amount of Fe isotopic fractionation (up to 0.3‰) between the host basalts ($+0.06$ to $+0.18\text{‰}$) and the vent fluids (-1.85 to -0.14‰) (Figure 2). This suggests that the Fe in the chalcopyrite was derived from the interaction between the hydrothermal fluid and the host basalt. As was previously observed by Rouxel et al. (2008), in the hydrothermal field of the EPR between 9°N and 10°N , the $\delta^{56}\text{Fe}$ values of chalcopyrite tend to be systematically more positive compared to those of coexisting pyrite and sphalerite (Table 2, Figure 6a), suggesting that a small amount of positive Fe isotopic fractionation occurs during chalcopyrite precipitation.

We also observed this phenomenon for the EPR between 1°S and 2°S , in the EHF on the CIR, and in S99HF on the NFB, where the $\delta^{56}\text{Fe}$ and $\delta^{57}\text{Fe}$ values of the chalcopyrite are significantly higher than those of the coexisting pyrite and sphalerite (Table 2, Figure 6a). This suggests that the Fe isotopes of the sulfides and fluids are in disequilibrium (Rouxel et al., 2008; Sharma et al., 2001), and that ^{56}Fe and ^{57}Fe are more likely to be incorporated into chalcopyrite under high-temperature fluid conditions (Butler and

Nesbitt, 1999). Thus, the high-temperature chalcopyrite is characterized by enriched $\delta^{56}\text{Fe}$ and $\delta^{57}\text{Fe}$ values (Figure 6a). Furthermore, the $\delta^{56}\text{Fe}$ values ($+0.11 \pm 0.09\text{‰}$) of the chalcopyrite from the hydrothermal field on the EPR between 1°S and 2°S are close to those of their host basalts ($+0.06$ to $+0.18\text{‰}$). This indicates that the Fe was mainly leached from local basaltic rocks and was incorporated into the chalcopyrite under high-temperature fluid conditions. Moreover, this means that no significant Fe isotopic fractionation occurred during the high-temperature basalt-fluid interactions.

The $\delta^{56}\text{Fe}$ values of the pyrite exhibit a large variation (-1.96 to $+0.11\text{‰}$) compared to those of the host basaltic rocks ($+0.06$ to $+0.18\text{‰}$), with large Fe isotopic fractionation (up to 2‰). This is consistent with the varying fluid temperatures, which ranged from high to low during the pyrite formation (Figure 6a) (Abraitis et al., 2004; Keith et al., 2016). These values are slightly lower than the $\delta^{56}\text{Fe}$ values of seawater (-0.88 to $+0.10\text{‰}$; Rouxel & Maureen, 2010) and are similar to the $\delta^{56}\text{Fe}$ variation in hydrothermal fluids (-1.85 to -0.14‰ ; Moeller et al., 2014; Rouxel et al., 2008; Severmann et al., 2004; Sharma et al., 2001) (Figure 2). All of these findings indicate that the fluids may be a source of the light Fe isotopic compositions of the sulfides, and that ^{54}Fe is more likely to be preferentially incorporated into pyrite facies during mixing between seawater and hydrothermal fluids. This suggests that low-temperature pyrite is characterized by depleted $\delta^{56}\text{Fe}$ and $\delta^{57}\text{Fe}$ values (Figure 6a).

Rouxel et al. (2008) reported that the relatively slow precipitation of pyrite in subsurface environments due to the conductive cooling of the fluids produces limited Fe isotopic fractionation, while the rapid precipitation of pyrite as a result of mixing in chimney environments produces significant kinetic Fe isotopic fractionation. Therefore, the large Fe isotopic variations of the sulfide minerals are likely to have been influenced by the precipitation rate. The Fe isotope results reveal that the chalcopyrite has systematically higher $\delta^{56}\text{Fe}$ values than the pyrite and sphalerite (Figure 2), which means that the pyrite, sphalerite, and chalcopyrite within a single hydrothermal field exhibit Fe isotope disequilibrium. Moreover, there is no clear relationship between the Fe isotopic compositions of the sulfides from the different ridge segments and the local MOR spreading rates (Figures 5a, S2), suggesting that the MOR spreading rate did not significantly affect the Fe isotopic compositions of the sulfide minerals in the local hydrothermal fields.

Furthermore, the sphalerite minerals from the EHF on the CIR and the S99HF on the NFB include small amounts of pyrite and chalcopyrite, and the $\delta^{56}\text{Fe}$ values of the sphalerite minerals from the EHF on the CIR and the S99HF on the NFB exhibit large variations (-1.65 to -0.63%) compared to those of the chalcopyrite minerals (Figure 2), implying that the Fe isotopic compositions of the sphalerite minerals are controlled by small pyrite and chalcopyrite inclusions, which can be used to trace the sulfide inclusions in the sphalerite minerals.

4.2.2 Cu Isotopes

The chalcopyrite from the sulfide samples have consistent depleted $\delta^{65}\text{Cu}$ values, with a smaller $\delta^{65}\text{Cu}$ variation range (-0.88 to -0.16%) than that of the Fe isotopes of the sulfide minerals and a small amount of Cu isotopic fractionation (up to 0.7%), which is significantly lower than that of the host MORBs and the hydrothermal fluids (Figure 3). This suggests that ^{63}Cu was preferentially removed from the hydrothermal fluid and was incorporated into the chalcopyrite during the formation of the chalcopyrite, and the heavier Cu isotope was more likely to remain in the high-temperature fluids from which the chalcopyrite precipitated (Figure 6b). This implies that the hydrothermal fluids, which have heavier Cu isotopic compositions, may provide a source of heavy Cu isotopes to hydrothermal plumes, seawater, and metalliferous sediments during fluid-seawater mixing and the settling of hydrothermal material.

This is consistent with the general observation of Zhu et al. (2000) regarding the EPR hydrothermal fields, in which the inactive sulfide deposits have more depleted $\delta^{65}\text{Cu}$ values than the active high-temperature hydrothermal vents, which have significantly lower values than the host MORBs (avg. of $+0.07 \pm 0.06\%$; Liu et al., 2015; Savage et al., 2015; this work) and the hydrothermal fluids ($+0.1$ to $+0.5\%$; Dekov and Rouxel, 2012) (Figure 3). This suggests that the Cu isotopes of the chalcopyrite and the hydrothermal fluid are in disequilibrium, and that significant Cu isotopic fractionation occurred

between the chalcopyrite and the hydrothermal fluid. This can be explained by the Cu isotopic exchange that occurs during redox processes and the precipitation of chalcopyrite. Furthermore, the hydrothermal processes did not lead to a large amount of Cu isotopic fractionation in the chalcopyrite, suggesting that direct precipitation in equilibrium with the end-member fluids produces positive Cu isotopic compositions, as opposed to the observed negative Cu isotopic compositions of the chalcopyrite.

However, sulfides that are crystallized during early stage hydrothermal processes are known to undergo extensive chemical and textural modifications during the subsequent hydrothermal diagenesis (Rouxel et al., 2004b, 2008; Sharma et al., 2001). This may lead to reactions between the $\delta^{65}\text{Cu}$ -depleted late-stage fluids and the early-formed sulfides to produce $\delta^{65}\text{Cu}$ -depleted sulfides (Zhu et al., 2000). Rouxel et al. (2004b) reported that hydrothermal sulfides characterized by negative $\delta^{65}\text{Cu}$ values have undergone extensive recrystallization. If heavy Cu isotopes are released during the reworking and/or alteration of chalcopyrite, the $\delta^{65}\text{Cu}$ values of the residual sulfides should become more negative as the replacement reactions proceed (Rouxel et al., 2004b). Therefore, the negative $\delta^{65}\text{Cu}$ values of the chalcopyrite from the sulfide samples in this study may be the product of replacement recrystallization via a reaction with later $\delta^{65}\text{Cu}$ -depleted fluids. This suggests that the ^{63}Cu in the hydrothermal fluids is more likely to be incorporated into the chalcopyrite facies during replacement recrystallization, and the Cu isotopic compositions of sulfides can be used to decipher the details of seafloor hydrothermal

redox processes. Furthermore, the MOR segments from which our hydrothermal sulfide samples were collected are sediment starved, making the incorporation of significant amounts of Cu originating from a sedimentary source unlikely. Moreover, the seawater exhibits a large range of heavier Cu isotope compositions (-0.18 to $+1.44\%$; Little et al., 2014; Vance et al., 2008) compared to the chalcopyrite in this study (Figure 3). The Cu concentration of the seawater is approximately 2×10^{-9} mol/kg (Wu & Boyle, 1997), which is significantly lower than that of the high-temperature hydrothermal fluids ($9.7\text{--}150 \times 10^{-6}$ mol/kg; Edmond et al., 1996; Elderfield & Schultz, 1996). Therefore, mixing between seawater and hydrothermal fluids or the mantle source cannot explain the observed negative Cu isotope compositions of the studied hydrothermal sulfides.

4.2.3 Zn Isotopes

In hydrothermal systems, Zn isotopes can also be used as tracers of seafloor hydrothermal processes, thereby increasing our understanding of the plumbing and chemistry of hydrothermal vents (John et al., 2008). Possible Zn isotope fractionation and the magnitude thereof should be considered prior to evaluating the potential of using Zn isotopes to trace the source of ore-forming metals. Several processes are considered to be potential causes of Zn isotope variations during ore-forming processes, including: (1) temperature effects (Mason et al., 2005; Toutain et al., 2008), (2) the mixing of multiple

zinc sources (Wilkinson et al., 2005; Zhou et al., 2014), and/or (3) kinetic Raleigh fractionation during mineral precipitation (Gagnevin et al., 2012; Kelley et al., 2009).

The $\delta^{66}\text{Zn}$ values of the sphalerite (-0.39 to -0.03‰) in this study are substantially lower than those of the host basalts ($>0.31\text{‰}$, Table 1) and the hydrothermal fluids ($+0.00$ to $+1.04\text{‰}$; John et al., 2008), which are in the range of seawater (Figure 4) (-0.33 to $+0.80\text{‰}$; Little et al., 2014; Samanta et al., 2017; Y. Zhao et al., 2014). This suggests that the Zn isotopes of the sphalerite and the hydrothermal fluids are in disequilibrium.

Significant Zn isotopic fractionation occurred between the sphalerite and the hydrothermal fluid due to the Zn isotopic exchange during fluid-seawater mixing and the sphalerite precipitation. However, the ^{64}Zn in the hydrothermal fluid was more likely to be incorporated into the sphalerite during the mixing of the seawater and hydrothermal fluid, resulting in the preferential enrichment of the heavier Zn isotopes in the hydrothermal fluids from which the sphalerite precipitated (Dekov & Rouxel, 2012).

This suggests that fluids with heavier Zn isotopic compositions can provide a source of heavy Zn isotopes to hydrothermal plumes, seawater, and metalliferous sediments during fluid-seawater mixing and the settling of hydrothermal material. Furthermore, equilibrium isotopic fractionation is a function of temperature, with larger amounts of fractionation occurring at lower temperatures (Urey, 1947). The experimental studies conducted by Maréchal and Sheppard (2002) demonstrated that limited Zn isotope variation occurs within a temperature range of $30\text{--}50^\circ\text{C}$. The fluid temperatures in the

EHF and NFB are 273–382°C (Gallant & Von Damm, 2006) and 285–291°C (Grimaud et al., 1991; Ishibashi, Grimaud, et al., 1994; Ishibashi, Wakita, et al., 1994), respectively. These results indicate that the deposition of the Zn in the sphalerite carried ^{66}Zn and ^{68}Zn out of the host basalts during the fluid-basalt interaction under medium- and/or low-temperature fluid conditions (Figure 6c), resulting in the preferential enrichment of the lighter Zn isotope in the hydrothermally altered basaltic rock during the host basalt-fluid interaction. This implies that the influence of a plate subduction component containing altered rocks on the magma source results in the preferential enrichment of the lighter Zn isotope in BAB and IA volcanic rocks. Furthermore, the $\delta^{66}\text{Zn}$ values of MORBs are slightly higher than those of OIBs (Figure 4), implying that the isotopic heterogeneity of the OIBs (Herzog et al., 2009; Teng et al., 2013) may be explained by hydrothermally altered oceanic crust (HAOC) with lower $\delta^{66}\text{Zn}$ values being injected into the OIB magma.

However, Rayleigh distillation can fractionate Zn isotopes in hydrothermal fluids, with $\delta^{66}\text{Zn}$ values increasing from the early to late stages, due to the precipitation of ^{64}Zn -enriched sulfides (such as sphalerite). John et al. (2008) reported that the subsurface precipitation of isotopically light Zn sulfides is the main cause of the isotopic variations in hydrothermal fluids. Moreover, several studies have identified or inferred the preferential incorporation of lighter Zn isotopes into Zn sulfide precipitates (e.g., Wilkinson et al., 2005), and laboratory experiments have also demonstrated that sulfide

precipitation is accompanied by the isotopic effects of $\Delta^{66}\text{Zn} = -0.36\text{‰}$ (Archer et al., 2004). Therefore, during the evolution of hydrothermal fluids, the precipitation of sulfides may cause Zn isotopic fractionation, with minerals being enriched in light Zn isotopes and the fluid being enriched in heavy Zn isotopes. Theoretical calculations indicated that Zn isotopic fractionation between an aqueous Zn solution and a sulfide species is 0.2‰ at approximately 300°C (Fujii et al., 2011). However, when the Zn isotopic fractionation between hydrothermal fluids and sulfides (0.2‰) is considered (Fujii et al., 2011), the $\delta^{66}\text{Zn}$ values of the hydrothermal fluids were calculated to be -0.06‰ and 0.00‰ for the EHF and S99HF, respectively. These values are lower than the measured $\delta^{66}\text{Zn}$ values of the hydrothermal fluids (0.00 to +1.33‰; John et al., 2008), implying that other sources with low $\delta^{66}\text{Zn}$ values were involved. According to Figure 4, seawater with low $\delta^{66}\text{Zn}$ values (-0.33 to +0.96‰; Little et al., 2014; Samanta et al., 2017; Y. Zhao et al., 2014) may be a suitable candidate to explain the low $\delta^{66}\text{Zn}$ values of the sphalerite. When hydrothermal fluids mix with seawater, additional isotopically light Zn is incorporated into the sulfide precipitates, which could account for the low $\delta^{66}\text{Zn}$ values of the sphalerite from the EHF and S99HF obtained in this study.

5. Conclusions

The Fe, Cu, and Zn isotopic compositions of the MORBs analyzed in this study

exhibit various $\delta^{56}\text{Fe}$ (+0.06 to +0.18‰), $\delta^{65}\text{Cu}$ (−0.10 to +0.73‰), and $\delta^{66}\text{Zn}$ (+0.31 to +0.51‰) ranges, which are beyond the range of previously studied MORBs. The $\delta^{66}\text{Zn}$ values of the MORBs are slightly higher than those of the OIBs due to the incorporation of HAOC into the OIB magma. However, unlike the Fe and Cu isotopes, the $\delta^{66}\text{Zn}$ values of the basalts exhibit an increasing trend, from the fast-spreading EPR to the intermediate-spreading CIR to the ultraslow-spreading SWIR, suggesting that ^{66}Zn is more likely to be incorporated into the basaltic magma under an ultraslow-spreading MOR, despite the fact that the Zn isotopic composition of the MOR mantle is heterogeneous. Furthermore, no relationship between the variations in the Fe and Cu isotopic compositions of the MORBs from the different ridge segments and the local spreading rate was identified, suggesting that the MOR spreading rate and the magmatic processes did not affect the Fe and Cu isotopic compositions of the MORBs. As with the Zn isotopic compositions, the varied Fe and Cu isotopic compositions of the studied MORBs could have resulted from the $\delta^{56}\text{Fe}$ and $\delta^{65}\text{Cu}$ heterogeneity of the mantle sources.

The $\delta^{56}\text{Fe}$ values of the MORS and BABS vary from −1.96 to +0.11‰, which is within the range of the hydrothermal fluids but is significantly lower than those of the host MORBs and BABBs, suggesting that the hydrothermal fluids could be a major source of the negative Fe isotopic compositions of the sulfides. However, Fe isotopic fractionation of up to 2‰ was observed for the pyrite precipitated from hydrothermal

fluids ranging from high to low temperatures, and the majority of the $\delta^{56}\text{Fe}$ and $\delta^{57}\text{Fe}$ values of the chalcopyrite are larger than those of the sphalerite and pyrite. This indicates that the high-temperature sulfides are characterized by enriched $\delta^{56}\text{Fe}$ and $\delta^{57}\text{Fe}$ values, while the medium- and low-temperature sulfides are characterized by depleted $\delta^{56}\text{Fe}$ and $\delta^{57}\text{Fe}$ values.

The chalcopyrite from the MORS and BABS have a smaller range of $\delta^{65}\text{Cu}$ values (-0.88 to -0.16‰) and less Cu isotopic fractionation (up to 0.7‰). These values are significantly lower than those of their host MORBs and hydrothermal fluids, suggesting the preferential enrichment of the heavier Cu isotopes in the hydrothermal fluids from which the chalcopyrite precipitated.

The sphalerite in the MORS and BABS exhibit a small range of $\delta^{66}\text{Zn}$ values (-0.39 to -0.03‰), with a small amount of Zn isotopic fractionation (up to 0.3‰). These values are also significantly lower than those of the host MORBs and hydrothermal fluids, which are in the range of seawater, suggesting that the Zn deposition during the sphalerite precipitation carried ^{64}Zn out of the hydrothermal fluids during seawater-hydrothermal fluid mixing under medium- and/or low-temperature conditions.

The ^{54}Fe in the basalts was more likely to be incorporated into the hydrothermal fluids during the fluid-basalt interactions, while the ^{64}Zn in the hydrothermal fluid was more likely to be incorporated into the sphalerite during seawater-hydrothermal fluid mixing. This resulted in the preferential enrichment of the heavier Zn isotope in the fluids;

739 thus, the heavier Fe and lighter Zn isotopic compositions of the altered rocks. This
740 implies that the influence of a plate subduction component containing hydrothermally
741 altered rocks on the BAB and IA magma sources results in the preferential enrichment of
742 heavier Fe and lighter Zn isotopes in BAB and IA volcanic rocks.

743 It is possible that hydrothermal fluids with heavier Cu and Zn isotopic compositions
744 result in the preferential enrichment of heavier Cu and Zn isotopes in hydrothermal
745 plumes, seawater, and metalliferous sediments during fluid-seawater mixing and the
746 settling of hydrothermal material. Moreover, the Cu and Zn isotopes of the sulfides and
747 the hydrothermal fluids are in disequilibrium, which can be explained by isotopic
748 exchange during the precipitation of the chalcopyrite and sphalerite. Furthermore,
749 significant Cu and Zn isotopic fractionation occurred between the hydrothermal fluid and
750 the precipitated sulfide minerals, and the redox processes, hydrothermal fluid-seawater
751 mixing, and the sulfide precipitation likely caused the Cu and Zn isotopic fractionations.
752 Our findings improve our understanding of the Fe, Cu, and Zn isotopic compositions of
753 sulfides and volcanic rocks as well as the mechanisms responsible for these compositions.
754 Moreover, they improve our understanding of the Fe, Cu, and Zn sources of sulfides, the
755 relationships between the sulfides and their host volcanic rocks, and the hydrothermal
756 processes involved in the transfer of Fe, Cu, and Zn between the mantle sources,
757 hydrothermal fluids, host rocks, and sulfides.

758

759

760 **Acknowledgements**

761 We would like to thank the crews of the DY105-17, DY115-19, DY115-20, and
762 DY115-21 cruises for their help with the sample collection. We are grateful to Dr. Erio
763 Rahders of the Institute for Geological Sciences, Geology Department, Free University of
764 Berlin, and Dr. Huaiming Li of the Second Institute of Oceanography, State Oceanic
765 Administration, China, for providing some of the samples. This work was supported by
766 the National Natural Science Foundation of China (91958213), the National Program on
767 Global Change and Air-Sea Interaction (GASI-GEOGE-02), the International Partnership
768 Program of the Chinese Academy of Sciences (133137KYSB20170003), the Taishan
769 Scholar Foundation of Shandong Province (ts201511061), the National Special Fund for
770 the 13th Five Year Plan of COMRA (DY135-G2-01-02), and the National Key Basic
771 Research Program of China (2013CB429700). We thank LetPub for its linguistic
772 assistance during the preparation of this manuscript.

773

774

775

776

777

778

779 **References**

- 780 Abraitis, P. K., Pattrick, R. A. D., & Vaughan, D. J. (2004). Variations in the
781 compositional, textural and electrical properties of natural pyrite: a review.
782 *International Journal of Mineral Processing*, 74(1–4), 41–59.
783 <https://dx.doi.org/10.1016/j.minpro.2003.09.002>
- 784 Anbar, A. D., Jarzecki, A. A., & Spiro, T. G. (2005). Theoretical investigation of iron
785 isotope fractionation between $\text{Fe}(\text{H}_2\text{O})_6^{3+}$ and $\text{Fe}(\text{H}_2\text{O})_6^{2+}$: implications for iron
786 stable isotope geochemistry. *Geochimica et Cosmochimica Acta*, 69(4), 825–837.
787 <https://dx.doi.org/10.1016/j.gca.2004.06.012>
- 788 Archer, C., & Vance, D. (2004). Mass discrimination correction in multiple-collector
789 plasma source mass spectrometry: an example using Cu and Zn isotopes. *Journal*
790 *of Analytical Atomic Spectrometry*, 19(5), 656–665.
791 <https://dx.doi.org/10.1039/b315853e>
- 792 Beard, B. L., Johnson, C. M., Skulan, J. L., Nealson, K. H., Cox, L., & Sun, H. (2003).
793 Application of Fe isotopes to tracing the geochemical and biological cycling of
794 Fe. *Chemical Geology*, 195(1–4), 87–117.
795 [https://dx.doi.org/10.1016/s0009-2541\(02\)00390-x](https://dx.doi.org/10.1016/s0009-2541(02)00390-x)
- 796 Beard, B. L., Johnson, C. M., Von Damm, K. L., & Poulson, R. L. (2003). Iron isotope
797 constraints on Fe cycling and mass balance in oxygenated Earth oceans. *Geology*,

798 31(7), 629–632.
799 [https://dx.doi.org/10.1130/0091-7613\(2003\)031<0629:iicofc>2.0.co;2](https://dx.doi.org/10.1130/0091-7613(2003)031<0629:iicofc>2.0.co;2)
800 Bennett, S. A., Rouxel, O., Schmidt, K., Garbe-Schönberg, D., Statham, P. J., & German,
801 C. R. (2009). Iron isotope fractionation in a buoyant hydrothermal plume, 5°S
802 Mid-Atlantic Ridge. *Geochimica et Cosmochimica Acta*, 73(19), 5619–5634.
803 <https://dx.doi.org/10.1016/j.gca.2009.06.027>
804 Ben Othman, D., Luck, J. M., Bodinier, J. L., Arndt, N. T., & Albarède, F. (2006). Cu–Zn
805 isotopic variations in the Earth’s mantle. *Geochimica et Cosmochimica Acta*,
806 70(S18), A46. <https://dx.doi.org/10.1016/j.gca.2006.06.201>
807 Bézoz, A., & Humler, E. (2005). The Fe³⁺/ΣFe ratios of MORB glasses and their
808 implications for mantle melting. *Geochimica et Cosmochimica Acta*, 69(3),
809 711–725. <https://dx.doi.org/10.1016/j.gca.2004.07.026>
810 Bluth, G. J., & Ohmoto, H. (1988). Sulfide-sulfate chimneys on the East Pacific Rise, 11
811 degrees and 13 degrees N latitudes; Part II, sulfur isotopes. *The Canadian*
812 *Mineralogist*, 26(3), 505–515.
813 Bowers, T. S., Campbell, A. C., Measures, C. I., Spivack, A. J., Khadem, M., & Edmond,
814 J. M. (1988). Chemical controls on the composition of vent fluids at 13°–11°N
815 and 21°N, East Pacific Rise. *Journal of Geophysical Research: Solid Earth*,
816 93(B5), 4522–4536. <https://dx.doi.org/10.1029/jb093ib05p04522>

817 Bullen, T. D., White, A. F., Childs, C. W., Vivit, D. V., & Schulz, M. S. (2001).
818 Demonstration of significant abiotic iron isotope fractionation in nature. *Geology*,
819 29(8), 699–702.
820 [https://dx.doi.org/10.1130/0091-7613\(2001\)029<0699:dosaii>2.0.co;2](https://dx.doi.org/10.1130/0091-7613(2001)029<0699:dosaii>2.0.co;2)

821 Butler, I. B., & Nesbitt, R. W. (1999). Trace element distributions in the chalcopyrite
822 wall of a black smoker chimney: insights from laser ablation inductively coupled
823 plasma mass spectrometry (LA–ICP–MS). *Earth and Planetary Science Letters*,
824 167(3–4), 335–345. [https://dx.doi.org/10.1016/s0012-821x\(99\)00038-2](https://dx.doi.org/10.1016/s0012-821x(99)00038-2)

825 Chen, H., Savage, P. S., Teng, F. Z., Helz, R. T., & Moynier, F. (2013). Zinc isotope
826 fractionation during magmatic differentiation and the isotopic composition of the
827 bulk Earth. *Earth and Planetary Science Letters*, 369–370, 34–42.
828 <https://dx.doi.org/10.1016/j.epsl.2013.02.037>

829 Christie, D. M., Carmichael, I. S. E., & Langmuir, C. H. (1986). Oxidation states of
830 mid-ocean ridge basalt glasses. *Earth and Planetary Science Letters*, 79(3–4),
831 397–411. [https://dx.doi.org/10.1016/0012-821x\(86\)90195-0](https://dx.doi.org/10.1016/0012-821x(86)90195-0)

832 Chu, N. C., Johnson, C. M., Beard, B. L., German, C. R., Nesbitt, R. W., Frank, M., et al.
833 (2006). Evidence for hydrothermal venting in Fe isotope compositions of the deep
834 Pacific Ocean through time. *Earth and Planetary Science Letters*, 245(1–2),
835 202–217. <https://dx.doi.org/10.1016/j.epsl.2006.02.043>

836 Chu, Z. Y., Wu, F. Y., Walker, R. J., Rudnick, R. L., Pitcher, L., Puchtel, I. S., et al.
837 (2009). Temporal evolution of the lithospheric mantle beneath the eastern North
838 China Craton. *Journal of Petrology*, 50(10), 1857–1898.
839 <https://dx.doi.org/10.1093/petrology/egp055>

840 Croal, L. R., Johnson, C. M., Beard, B. L., & Newman, D. K. (2004). Iron isotope
841 fractionation by Fe(II)-oxidizing photoautotrophic bacteria. *Geochimica et*
842 *Cosmochimica Acta*, 68(6), 1227–1242.
843 <https://dx.doi.org/10.1016/j.gca.2003.09.011>

844 Dasgupta, R., Jackson, M. G., & Lee, C. T. A. (2010). Major element chemistry of ocean
845 island basalts—conditions of mantle melting and heterogeneity of mantle source.
846 *Earth and Planetary Science Letters*, 289(3–4), 377–392.
847 <https://dx.doi.org/10.1016/j.epsl.2009.11.027>

848 Dauphas, N., Craddock, P. R., Asimow, P. D., Bennett, V. C., Nutman, A. P., &
849 Ohnenstetter, D. (2009). Iron isotopes may reveal the redox conditions of mantle
850 melting from Archean to present. *Earth and Planetary Science Letters*, 288(1–2),
851 255–267. <https://dx.doi.org/10.1016/j.epsl.2009.09.029>

852 Dauphas, N., & Rouxel, O. (2006). Mass spectrometry and natural variations of iron
853 isotopes. *Mass Spectrometry Reviews*, 25(4), 515–550.
854 <https://dx.doi.org/10.1002/mas.20078>

855 Davis, F. A., Humayun, M., Hirschmann, M. M., & Cooper, R. S. (2013). Experimentally
856 determined mineral/melt partitioning of first-row transition elements (FRTE)
857 during partial melting of peridotite at 3GPa. *Geochimica et Cosmochimica Acta*,
858 *104*, 232–260. <https://dx.doi.org/10.1016/j.gca.2012.11.009>

859 Debret, B., Beunon, H., Mattielli, N., Andreani, M., Ribeiro da Costa, I., & Escartin, J.
860 (2018). Ore component mobility, transport and mineralization at mid-oceanic
861 ridges: a stable isotopes (Zn, Cu and Fe) study of the Rainbow massif
862 (Mid-Atlantic Ridge 36°14'N). *Earth and Planetary Science Letters*, *503*,
863 170–180. <https://dx.doi.org/10.1016/j.epsl.2018.09.009>

864 Dekov, V., & Rouxel, O. (2012). *Cu- and Zn-isotope systematics of seafloor*
865 *hydrothermal vent fluids from a back-arc setting (Manus Basin)*. Paper presented
866 at EGU General Assembly 2012, European Geosciences Union, Vienna, Austria.

867 DeMets, C., Gordon, R. G., Argus, D. F., & Stein, S. (1994). Effect of recent revisions to
868 the geomagnetic reversal time scale on estimates of current plate motions.
869 *Geophysical Research Letters*, *21*(20), 2191–2194.
870 <https://dx.doi.org/10.1029/94gl02118>

871 Doucet, L. S., Mattielli, N., Ionov, D. A., Debouge, W., & Golovin, A. V. (2016). Zn
872 isotopic heterogeneity in the mantle: a melting control? *Earth and Planetary*
873 *Science Letters*, *451*, 232–240. <https://dx.doi.org/10.1016/j.epsl.2016.06.040>

874 Edmonds, H. N., German, C. R., Green, D. R. H., Huh, Y., Gamo, T., & Edmond, J. M.
875 (1996). Continuation of the hydrothermal fluid chemistry time series at TAG, and
876 the effects of ODP drilling. *Geophysical Research Letters*, 23(23), 3487–3489.
877 <https://dx.doi.org/10.1029/96gl01597>

878 Eissen, J. P., Nohara, M., Cotten, J., & Hirose, K. (1994). North Fiji Basin basalts and
879 their magma sources: part I. incompatible element constraints. *Marine Geology*,
880 116(1–2), 153–178. [https://dx.doi.org/10.1016/0025-3227\(94\)90174-0](https://dx.doi.org/10.1016/0025-3227(94)90174-0)

881 Elderfield, H., & Schultz, A. (1996). Mid-ocean ridge hydrothermal fluxes and the
882 chemical composition of the ocean. *Annual Review of Earth and Planetary*
883 *Sciences*, 24, 191–224. <https://dx.doi.org/10.1146/annurev.earth.24.1.191>

884 Fernandez, A., & Borrok, D. M. (2009). Fractionation of Cu, Fe, and Zn isotopes during
885 the oxidative weathering of sulfide-rich rocks. *Chemical Geology*, 264(1–4), 1–12.
886 <https://dx.doi.org/10.1016/j.chemgeo.2009.01.024>

887 Foustoukos, D. I., & Seyfried, W. E. (2007). Quartz solubility in the two-phase and
888 critical region of the NaCl–KCl–H₂O system: implications for submarine
889 hydrothermal vent systems at 9°50'N East Pacific Rise. *Geochimica et*
890 *Cosmochimica Acta*, 71(1), 186–201.
891 <https://dx.doi.org/10.1016/j.gca.2006.08.038>

892 Frost, D. J., & McCammon, C. A. (2008). The redox state of Earth's mantle. *Annual*
893 *Review of Earth and Planetary Sciences*, 36, 389–420.
894 <https://dx.doi.org/10.1146/annurev.earth.36.031207.124322>

895 Fujii, T., Moynier, F., Pons, M. L., & Albarède, F. (2011). The origin of Zn isotope
896 fractionation in sulfides. *Geochimica et Cosmochimica Acta*, 75(23), 7632–7643.
897 <https://dx.doi.org/10.1016/j.gca.2011.09.036>

898 Gagnevin, D., Boyce, A. J., Barrie, C. D., Menuge, J. F., & Blakeman, R. J. (2012). Zn,
899 Fe and S isotope fractionation in a large hydrothermal system. *Geochimica et*
900 *Cosmochimica Acta*, 88, 183–198. <https://dx.doi.org/10.1016/j.gca.2012.04.031>

901 Gallant, R. M., & Von Damm, K. L. (2006). Geochemical controls on hydrothermal
902 fluids from the Kairei and Edmond Vent Fields, 23°–25°S, Central Indian Ridge.
903 *Geochemistry, Geophysics, Geosystems*, 7(6), Q06018.
904 <https://dx.doi.org/10.1029/2005gc001067>

905 German, C. R., Bennett, S. A., Connelly, D. P., Evans, A. J., Murton, B. J., Parson, L. M.,
906 et al. (2008). Hydrothermal activity on the southern Mid-Atlantic Ridge:
907 tectonically- and volcanically-controlled venting at 4–5°S. *Earth and Planetary*
908 *Science Letters*, 273(3–4), 332–344. <https://dx.doi.org/10.1016/j.epsl.2008.06.048>

909 Grimaud, D., Ishibashi, J. I., Lagabriele, Y., Auzende, J. M., & Urabe, T. (1991).
910 Chemistry of hydrothermal fluids from the 17°S active site on the North Fiji

911 Basin Ridge (SW Pacific). *Chemical Geology*, 93(3–4), 209–218.
912 [https://dx.doi.org/10.1016/0009-2541\(91\)90114-7](https://dx.doi.org/10.1016/0009-2541(91)90114-7)

913 Heimann, A., Beard, B. L., & Johnson, C. M. (2008). The role of volatile exsolution and
914 sub-solidus fluid/rock interactions in producing high $^{56}\text{Fe}/^{54}\text{Fe}$ ratios in siliceous
915 igneous rocks. *Geochimica et Cosmochimica Acta*, 72(17), 4379–4396.
916 <https://dx.doi.org/10.1016/j.gca.2008.06.009>

917 Herzog, G. F., Moynier, F., Albarède, F., & Berezhnoy, A. A. (2009). Isotopic and
918 elemental abundances of copper and zinc in lunar samples, Zagami, Pele’s hairs,
919 and a terrestrial basalt. *Geochimica et Cosmochimica Acta*, 73(19), 5884–5904.
920 <https://dx.doi.org/10.1016/j.gca.2009.05.067>

921 Hibbert, K. E. J., Williams, H. M., Kerr, A. C., & Puchtel, I. S. (2012). Iron isotopes in
922 ancient and modern komatiites: evidence in support of an oxidised mantle from
923 Archean to present. *Earth and Planetary Science Letters*, 321–322, 198–207.
924 <https://dx.doi.org/10.1016/j.epsl.2012.01.011>

925 Hofmann, A. W. (1997). Mantle geochemistry: the message from oceanic volcanism.
926 *Nature*, 385(6613), 219–229. <https://dx.doi.org/10.1038/385219a0>

927 Huang, J., Liu, S. A., Gao, Y., Xiao, Y., & Chen, S. (2016). Copper and zinc isotope
928 systematics of altered oceanic crust at IODP Site 1256 in the eastern equatorial
929 Pacific. *Journal of Geophysical Research: Solid Earth*, 121(10), 7086–7100.
930 <https://dx.doi.org/10.1002/2016jb013095>

931 Ionov, D. A., Doucet, L. S., & Ashchepkov, I. V. (2010). Composition of the lithospheric
 932 mantle in the Siberian craton: new constraints from fresh peridotites in the
 933 Udachnaya-East kimberlite. *Journal of Petrology*, 51(11), 2177–2210.
 934 <https://dx.doi.org/10.1093/petrology/egq053>

935 Ishibashi, J. I., Grimaud, D., Nojiri, Y., Auzende, J. M., & Urabe, T. (1994). Fluctuation
 936 of chemical compositions of the phase-separated hydrothermal fluid from the
 937 North Fiji Basin Ridge. *Marine Geology*, 116(1–2), 215–226.
 938 [https://dx.doi.org/10.1016/0025-3227\(94\)90177-5](https://dx.doi.org/10.1016/0025-3227(94)90177-5)

939 Ishibashi, J. I., Wakita, H., Nojiri, Y., Grimaud, D., Jean-Baptiste, P., Gamo, T., et al.
 940 (1994). Helium and carbon geochemistry of hydrothermal fluids from the North
 941 Fiji Basin spreading ridge (southwest Pacific). *Earth and Planetary Science*
 942 *Letters*, 128(3–4), 183–197. [https://dx.doi.org/10.1016/0012-821x\(94\)90144-9](https://dx.doi.org/10.1016/0012-821x(94)90144-9)

943 Ji, F., Zhou, H., Yang, Q., Gao, H., Wang, H., & Lilley, M. D. (2017). Geochemistry of
 944 hydrothermal vent fluids and its implications for subsurface processes at the
 945 active Longqi hydrothermal field, Southwest Indian Ridge. *Deep Sea Research*
 946 *Part I: Oceanographic Research Papers*, 122, 41–47.
 947 <https://dx.doi.org/10.1016/j.dsr.2017.02.001>

948 John, S. G., Rouxel, O. J., Craddock, P. R., Engwall, A. M., & Boyle, E. A. (2008). Zinc
 949 stable isotopes in seafloor hydrothermal vent fluids and chimneys. *Earth and*

950 *Planetary Science Letters*, 269(1–2), 17–28.

951 <https://dx.doi.org/10.1016/j.epsl.2007.12.011>

952 Johnson, C. M., Beard, B. L., Beukes, N. J., Klein, C., & O'Leary, J. M. (2003). Ancient

953 geochemical cycling in the Earth as inferred from Fe isotope studies of banded

954 iron formations from the Transvaal Craton. *Contributions to Mineralogy and*

955 *Petrology*, 144(5), 523–547. <https://dx.doi.org/10.1007/s00410-002-0418-x>

956 Johnson, C. M., Skulan, J. L., Beard, B. L., Sun, H., Nealson, K. H., & Braterman, P. S.

957 (2002). Isotopic fractionation between Fe(III) and Fe(II) in aqueous solutions.

958 *Earth and Planetary Science Letters*, 195(1–2), 141–153.

959 [https://dx.doi.org/10.1016/s0012-821x\(01\)00581-7](https://dx.doi.org/10.1016/s0012-821x(01)00581-7)

960 Keith, M., Häckel, F., Haase, K. M., Schwarz-Schampera, U., & Klemm, R. (2016). Trace

961 element systematics of pyrite from submarine hydrothermal vents. *Ore Geology*

962 *Reviews*, 72, 728–745. <https://dx.doi.org/10.1016/j.oregeorev.2015.07.012>

963 Kelley, K. D., Wilkinson, J. J., Chapman, J. B., Crowther, H. L., & Weiss, D. J. (2009).

964 Zinc isotopes in sphalerite from base metal deposits in the Red Dog district,

965 northern Alaska. *Economic Geology*, 104(6), 767–773.

966 <https://dx.doi.org/10.2113/gsecongeo.104.6.767>

967 Kim, J., Lee, I., Halbach, P., Lee, K. Y., Ko, Y. T., & Kim, K. H. (2006). Formation of

968 hydrothermal vents in the North Fiji Basin: sulfur and lead isotope constraints.

969 *Chemical Geology*, 233(3–4), 257–275.
970 <https://dx.doi.org/10.1016/j.chemgeo.2006.03.011>

971 Kim, J., Moon, J. W., Lee, I., Kim, Y., & Larson, P. (2014). *Copper isotope composition*
972 *of seafloor hydrothermal vents in back-arc and arc settings, western Pacific*.
973 Paper presented at Goldschmidt Conference 2014, Geochemical Society and
974 European Association of Geochemistry, Sacramento, CA.

975 Klein, E. M., & Langmuir, C. H. (1987). Global correlations of ocean ridge basalt
976 chemistry with axial depth and crustal thickness. *Journal of Geophysical*
977 *Research: Solid Earth*, 92(B8), 8089–8115.
978 <https://dx.doi.org/10.1029/jb092ib08p08089>

979 Koschinsky, A., Seifert, R., Halbach, P., Bau, M., Brasse, S., de Carvalho, L. M., &
980 Fonseca, N. M. (2002). Geochemistry of diffuse low-temperature hydrothermal
981 fluids in the North Fiji basin. *Geochimica et Cosmochimica Acta*, 66(8),
982 1409–1427. [https://dx.doi.org/10.1016/s0016-7037\(01\)00855-9](https://dx.doi.org/10.1016/s0016-7037(01)00855-9)

983 Kumagai, H., Nakamura, K., Toki, T., Morishita, T., Okino, K., Ishibashi, J. i., et al.
984 (2008). Geological background of the Kairei and Edmond hydrothermal fields
985 along the Central Indian Ridge: Implications of their vent fluids' distinct
986 chemistry. *Geofluids*, 8(4), 239–251.
987 <https://dx.doi.org/10.1111/j.1468-8123.2008.00223.x>

988 Kunzmann, M., Halverson, G. P., Sossi, P. A., Raub, T. D., Payne, J. L., & Kirby, J.
989 (2013). Zn isotope evidence for immediate resumption of primary productivity
990 after snowball Earth. *Geology*, 41(1), 27–30. <https://dx.doi.org/10.1130/g33422.1>

991 Le Roux, V., Dasgupta, R., & Lee, C. T. A. (2011). Mineralogical heterogeneities in the
992 Earth's mantle: constraints from Mn, Co, Ni and Zn partitioning during partial
993 melting. *Earth and Planetary Science Letters*, 307(3–4), 395–408.
994 <https://dx.doi.org/10.1016/j.epsl.2011.05.014>

995 Li, W., Jackson, S. E., Pearson, N. J., Alard, O., & Chappell, B. W. (2009). The Cu
996 isotopic signature of granites from the Lachlan Fold Belt, SE Australia. *Chemical*
997 *Geology*, 258(1–2), 38–49. <https://dx.doi.org/10.1016/j.chemgeo.2008.06.047>

998 Little, S. H., Vance, D., Walker-Brown, C., & Landing, W. M. (2014). The oceanic mass
999 balance of copper and zinc isotopes, investigated by analysis of their inputs, and
1000 outputs to ferromanganese oxide sediments. *Geochimica et Cosmochimica Acta*,
1001 125, 673–693. <https://dx.doi.org/10.1016/j.gca.2013.07.046>

1002 Liu, S. A., Huang, J., Liu, J., Wörner, G., Yang, W., Tang, Y. J., et al. (2015). Copper
1003 isotopic composition of the silicate Earth. *Earth and Planetary Science Letters*,
1004 427, 95–103. <https://dx.doi.org/10.1016/j.epsl.2015.06.061>

1005 Liu, S. A., Wang, Z. Z., Li, S. G., Huang, J., & Yang, W. (2016). Zinc isotope evidence
1006 for a large-scale carbonated mantle beneath eastern China. *Earth and Planetary*
1007 *Science Letters*, 444, 169–178. <https://dx.doi.org/10.1016/j.epsl.2016.03.051>

1008 Lodders, K. (2003). Solar system abundances and condensation temperatures of the
1009 elements. *The Astrophysical Journal*, 591(2), 1220–1247.
1010 <https://dx.doi.org/10.1086/375492>

1011 Maréchal, C. N., & Sheppard, S. M. F. (2002). Isotopic fractionation of Cu and Zn
1012 between chloride and nitrate solutions and malachite or smithsonite at 30° and
1013 50°C. *Geochimica et Cosmochimica Acta*, 66(S1), A84.
1014 [https://dx.doi.org/10.1016/S0016-7037\(02\)01007-4](https://dx.doi.org/10.1016/S0016-7037(02)01007-4)

1015 Maréchal, C. N., Télouk, P., & Albarède, F. (1999). Precise analysis of copper and zinc
1016 isotopic compositions by plasma-source mass spectrometry. *Chemical Geology*,
1017 156(1–4), 251–273. [https://dx.doi.org/10.1016/s0009-2541\(98\)00191-0](https://dx.doi.org/10.1016/s0009-2541(98)00191-0)

1018 Markl, G., Lahaye, Y., & Schwinn, G. (2006). Copper isotopes as monitors of redox
1019 processes in hydrothermal mineralization. *Geochimica et Cosmochimica Acta*,
1020 70(16), 4215–4228. <https://dx.doi.org/10.1016/j.gca.2006.06.1369>

1021 Mason, T. F. D., Weiss, D. J., Chapman, J. B., Wilkinson, J. J., Tessalina, S. G., Spiro,
1022 B., et al. (2005). Zn and Cu isotopic variability in the Alexandrinka
1023 volcanic-hosted massive sulphide (VHMS) ore deposit, Urals, Russia. *Chemical*
1024 *Geology*, 221(3–4), 170–187. <https://dx.doi.org/10.1016/j.chemgeo.2005.04.011>

1025 Merlivat, L., Pineau, F., & Javoy, M. (1987). Hydrothermal vent waters at 13°N on the
1026 East Pacific Rise: isotopic composition and gas concentration. *Earth and*

1027 *Planetary Science Letters*, 84(1), 100–108.

1028 [https://dx.doi.org/10.1016/0012-821x\(87\)90180-4](https://dx.doi.org/10.1016/0012-821x(87)90180-4)

1029 Michard, G., Albarède, F., Michard, A., Minster, J. F., Charlou, J. L., & Tan, N. (1984).

1030 Chemistry of solutions from the 13°N East Pacific Rise hydrothermal site. *Earth*

1031 *and Planetary Science Letters*, 67(3), 297–307.

1032 [https://dx.doi.org/10.1016/0012-821x\(84\)90169-9](https://dx.doi.org/10.1016/0012-821x(84)90169-9)

1033 Moeller, K., Schoenberg, R., Grenne, T., Thorseth, I. H., Drost, K., & Pedersen, R. B.

1034 (2014). Comparison of iron isotope variations in modern and Ordovician siliceous

1035 Fe oxyhydroxide deposits. *Geochimica et Cosmochimica Acta*, 126, 422–440.

1036 <https://dx.doi.org/10.1016/j.gca.2013.11.018>

1037 Moeller, K., Schoenberg, R., Pedersen, R. B., Weiss, D., & Dong, S. (2012). Calibration

1038 of the new certified reference materials ERM-AE633 and ERM-AE647 for copper

1039 and IRMM-3702 for zinc isotope amount ratio determinations. *Geostandards and*

1040 *Geoanalytical Research*, 36(2), 177–199.

1041 <https://dx.doi.org/10.1111/j.1751-908x.2011.00153.x>

1042 Nohara, M., Hirose, K., Eissen, J. P., Urabe, T., & Joshima, M. (1994). The North Fiji

1043 Basin basalts and their magma sources: part II. Sr-Nd isotopic and trace element

1044 constraints. *Marine Geology*, 116(1–2), 179–195.

1045 [https://dx.doi.org/10.1016/0025-3227\(94\)90175-9](https://dx.doi.org/10.1016/0025-3227(94)90175-9)

1046 Oosting, S. E., & Von Damm, K. L. (1996). Bromide/chloride fractionation in seafloor
1047 hydrothermal fluids from 9–10°N East Pacific Rise. *Earth and Planetary Science*
1048 *Letters*, 144(1–2), 133–145. [https://dx.doi.org/10.1016/0012-821x\(96\)00149-5](https://dx.doi.org/10.1016/0012-821x(96)00149-5)
1049 Patriat, P., & Segoufin, J. (1988). Reconstruction of the Central Indian Ocean.
1050 *Tectonophysics*, 155(1–4), 211–234.
1051 [https://dx.doi.org/10.1016/0040-1951\(88\)90267-3](https://dx.doi.org/10.1016/0040-1951(88)90267-3)
1052 Pękala, M., Asael, D., Butler, I. B., Matthews, A., & Rickard, D. (2011). Experimental
1053 study of Cu isotope fractionation during the reaction of aqueous Cu(II) with Fe(II)
1054 sulphides at temperatures between 40 and 200°C. *Chemical Geology*, 289(1–2),
1055 31–38. <https://dx.doi.org/10.1016/j.chemgeo.2011.07.004>
1056 Petit, J. C. J., de Jong, J., Chou, L., & Mattielli, N. (2008). Development of Cu and Zn
1057 isotope MC-ICP-MS measurements: application to suspended particulate matter
1058 and sediments from the Scheldt estuary. *Geostandards and Geoanalytical*
1059 *Research*, 32(2), 149–166. <https://dx.doi.org/10.1111/j.1751-908x.2008.00867.x>
1060 Pichat, S., Douchet, C., & Albarède, F. (2003). Zinc isotope variations in deep-sea
1061 carbonates from the eastern equatorial Pacific over the last 175 ka. *Earth and*
1062 *Planetary Science Letters*, 210(1–2), 167–178.
1063 [https://dx.doi.org/10.1016/s0012-821x\(03\)00106-7](https://dx.doi.org/10.1016/s0012-821x(03)00106-7)

1064 Poitrasson, F., & Freydier, R. (2005). Heavy iron isotope composition of granites
1065 determined by high resolution MC-ICP-MS. *Chemical Geology*, 222(1–2),
1066 132–147. <https://dx.doi.org/10.1016/j.chemgeo.2005.07.005>

1067 Polyakov, V. B., & Mineev, S. D. (2000). The use of Mössbauer spectroscopy in stable
1068 isotope geochemistry. *Geochimica et Cosmochimica Acta*, 64(5), 849–865.
1069 [https://dx.doi.org/10.1016/s0016-7037\(99\)00329-4](https://dx.doi.org/10.1016/s0016-7037(99)00329-4)

1070 Polyakov, V. B., & Soultanov, D. (2010). *Iron isotope fractionation in sulfide:*
1071 *constraints on mechanisms of sulfide formations in hydrothermal and magmatic*
1072 *systems*. Paper presented at EGU General Assembly 2010, European Geosciences
1073 Union, Vienna, Austria.

1074 Ponzevera, E., Quétel, C. R., Berglund, M., Taylor, P. D. P., Evans, P., Loss, R. D., &
1075 Fortunato, G. (2006). Mass discrimination during MC-ICPMS isotopic ratio
1076 measurements: investigation by means of synthetic isotopic mixtures (IRMM-007
1077 series) and application to the calibration of natural-like zinc materials (including
1078 IRMM-3702 and IRMM-651). *Journal of the American Society for Mass*
1079 *Spectrometry*, 17(10), 1413–1427. <https://dx.doi.org/10.1016/j.jasms.2006.06.001>

1080 Proskurowski, G., Lilley, M. D., & Olson, E. J. (2008). Stable isotopic evidence in
1081 support of active microbial methane cycling in low-temperature diffuse flow vents
1082 at 9°50'N East Pacific Rise. *Geochimica et Cosmochimica Acta*, 72(8),
1083 2005–2023. <https://dx.doi.org/10.1016/j.gca.2008.01.025>

1084 Prytulak, J., & Elliott, T. (2007). TiO₂ enrichment in ocean island basalts. *Earth and*
1085 *Planetary Science Letters*, 263(3–4), 388–403.
1086 <https://dx.doi.org/10.1016/j.epsl.2007.09.015>

1087 Reisberg, L., Zhi, X., Lorand, J. P., Wagner, C., Peng, Z., & Zimmermann, C. (2005).
1088 Re–Os and S systematics of spinel peridotite xenoliths from east central China:
1089 evidence for contrasting effects of melt percolation. *Earth and Planetary Science*
1090 *Letters*, 239(3–4), 286–308. <https://dx.doi.org/10.1016/j.epsl.2005.09.010>

1091 Rouxel, O., & Auro, M. (2010). Iron isotope variations in coastal seawater determined by
1092 multicollector ICP-MS. *Geostandards and Geoanalytical Research*, 34(2),
1093 135–144. <https://dx.doi.org/10.1111/j.1751-908x.2010.00063.x>

1094 Rouxel, O., Dobbek, N., Ludden, J., & Fouquet, Y. (2003). Iron isotope fractionation
1095 during oceanic crust alteration. *Chemical Geology*, 202(1–2), 155–182.
1096 <https://dx.doi.org/10.1016/j.chemgeo.2003.08.011>

1097 Rouxel, O., Fouquet, Y., & Ludden, J. N. (2004a). Copper isotope systematics of the
1098 Lucky Strike, Rainbow, and Logatchev sea-floor hydrothermal fields on the
1099 Mid-Atlantic Ridge. *Economic Geology*, 99(3), 585–600.
1100 <https://dx.doi.org/10.2113/gsecongeo.99.3.585>

1101 Rouxel, O., Fouquet, Y., & Ludden, J. N. (2004b). Subsurface processes at the lucky
1102 strike hydrothermal field, Mid-Atlantic ridge: evidence from sulfur, selenium, and

1103 iron isotopes. *Geochimica et Cosmochimica Acta*, 68(10), 2295–2311.

1104 <https://dx.doi.org/10.1016/j.gca.2003.11.029>

1105 Rouxel, O., Shanksiii, W., Bach, W., & Edwards, K. J. (2008). Integrated Fe- and

1106 S-isotope study of seafloor hydrothermal vents at East Pacific Rise 9–10°N.

1107 *Chemical Geology*, 252(3–4), 214–227.

1108 <https://dx.doi.org/10.1016/j.chemgeo.2008.03.009>

1109 Salters, V. J. M., Mallick, S., Hart, S. R., Langmuir, C. E., & Stracke, A. (2011).

1110 Domains of depleted mantle: new evidence from hafnium and neodymium

1111 isotopes. *Geochemistry, Geophysics, Geosystems*, 12(8), Q08001.

1112 <https://dx.doi.org/10.1029/2011gc003617>

1113 Samanta, M., Ellwood, M. J., Sinoir, M., & Hassler, C. S. (2017). Dissolved zinc isotope

1114 cycling in the Tasman Sea, SW Pacific Ocean. *Marine Chemistry*, 192, 1–12.

1115 <https://dx.doi.org/10.1016/j.marchem.2017.03.004>

1116 Savage, P. S., Harvey, J., & Moynier, F. (2014). *Copper isotope heterogeneity in the*

1117 *lithospheric mantle*. Paper presented at Goldschmidt Conference 2014,

1118 Geochemical Society and European Association of Geochemistry, Sacramento,

1119 CA.

1120 Savage, P. S., Moynier, F., Chen, H., Shofner, G., Siebert, J., Badro, J., & Puchtel, I. S.

1121 (2015). Copper isotope evidence for large-scale sulphide fractionation during

1122 Earth's differentiation. *Geochemical Perspectives Letters*, 1(1), 53–64.
1123 <https://dx.doi.org/10.7185/geochemlet.1506>

1124 Schauble, E. A., Rossman, G. R., & Taylor, H. P. (2001). Theoretical estimates of
1125 equilibrium Fe-isotope fractionations from vibrational spectroscopy. *Geochimica*
1126 *et Cosmochimica Acta*, 65(15), 2487–2497.
1127 [https://dx.doi.org/10.1016/s0016-7037\(01\)00600-7](https://dx.doi.org/10.1016/s0016-7037(01)00600-7)

1128 Schmidt, K., Koschinsky, A., Garbe-Schönberg, D., de Carvalho, L. M., & Seifert, R.
1129 (2007). Geochemistry of hydrothermal fluids from the ultramafic-hosted
1130 Logatchev hydrothermal field, 15°N on the Mid-Atlantic Ridge: temporal and
1131 spatial investigation. *Chemical Geology*, 242(1–2), 1–21.
1132 <https://dx.doi.org/10.1016/j.chemgeo.2007.01.023>

1133 Schoenberg, R., & von Blanckenburg, F. (2006). Modes of planetary-scale Fe isotope
1134 fractionation. *Earth and Planetary Science Letters*, 252(3–4), 342–359.
1135 <https://dx.doi.org/10.1016/j.epsl.2006.09.045>

1136 Schuessler, J. A., Schoenberg, R., & Sigmarsson, O. (2009). Iron and lithium isotope
1137 systematics of the Hekla volcano, Iceland—evidence for Fe isotope fractionation
1138 during magma differentiation. *Chemical Geology*, 258(1–2), 78–91.
1139 <https://dx.doi.org/10.1016/j.chemgeo.2008.06.021>

1140 Searle, R. C. (1983). Multiple, closely spaced transform faults in fast-slipping fracture
1141 zones. *Geology*, *11*(10), 607–610.
1142 [https://dx.doi.org/10.1130/0091-7613\(1983\)11<607:mcstfi>2.0.co;2](https://dx.doi.org/10.1130/0091-7613(1983)11<607:mcstfi>2.0.co;2)

1143 Severmann, S., Johnson, C. M., Beard, B. L., German, C. R., Edmonds, H. N., Chiba, H.,
1144 & Green, D. R. H. (2004). The effect of plume processes on the Fe isotope
1145 composition of hydrothermally derived Fe in the deep ocean as inferred from the
1146 Rainbow vent site, Mid-Atlantic Ridge, 36°14'N. *Earth and Planetary Science*
1147 *Letters*, *225*(1–2), 63–76. <https://dx.doi.org/10.1016/j.epsl.2004.06.001>

1148 Sharma, M., Polizzotto, M., & Anbar, A. D. (2001). Iron isotopes in hot springs along the
1149 Juan de Fuca Ridge. *Earth and Planetary Science Letters*, *194*(1–2), 39–51.
1150 [https://dx.doi.org/10.1016/s0012-821x\(01\)00538-6](https://dx.doi.org/10.1016/s0012-821x(01)00538-6)

1151 Shields, W. R., Goldich, S. S., Garner, E. L., & Murphy, T. J. (1965). Natural variations
1152 in the abundance ratio and the atomic weight of copper. *Journal of Geophysical*
1153 *Research*, *70*(2), 479–491. <https://dx.doi.org/10.1029/jz070i002p00479>

1154 Sossi, P. A., Halverson, G. P., Nebel, O., & Eggins, S. M. (2015). Combined separation
1155 of Cu, Fe and Zn from rock matrices and improved analytical protocols for stable
1156 isotope determination. *Geostandards and Geoanalytical Research*, *39*(2),
1157 129–149. <https://dx.doi.org/10.1111/j.1751-908x.2014.00298.x>

1158 Stracke, A., Hofmann, A. W., & Hart, S. R. (2005). FOZO, HIMU, and the rest of the
1159 mantle zoo. *Geochemistry, Geophysics, Geosystems*, 6(5), Q05007.
1160 <https://dx.doi.org/10.1029/2004gc000824>

1161 Taylor, P. D. P., Maeck, R., & De Bièvre, P. (1992). Determination of the absolute
1162 isotopic composition and Atomic Weight of a reference sample of natural iron.
1163 *International Journal of Mass Spectrometry and Ion Processes*, 121(1–2),
1164 111–125. [https://dx.doi.org/10.1016/0168-1176\(92\)80075-c](https://dx.doi.org/10.1016/0168-1176(92)80075-c)

1165 Telus, M., Dauphas, N., Moynier, F., Tissot, F. L. H., Teng, F. Z., Nabelek, P. I., et al.
1166 (2012). Iron, zinc, magnesium and uranium isotopic fractionation during
1167 continental crust differentiation: the tale from migmatites, granitoids, and
1168 pegmatites. *Geochimica et Cosmochimica Acta*, 97, 247–265.
1169 <https://dx.doi.org/10.1016/j.gca.2012.08.024>

1170 Teng, F. Z., Dauphas, N., & Helz, R. T. (2008). Iron isotope fractionation during
1171 magmatic differentiation in Kilauea Iki lava lake. *Science*, 320(5883), 1620–1622.
1172 <https://dx.doi.org/10.1126/science.1157166>

1173 Teng, F. Z., Dauphas, N., Helz, R. T., Gao, S., & Huang, S. (2011). Diffusion-driven
1174 magnesium and iron isotope fractionation in Hawaiian olivine. *Earth and*
1175 *Planetary Science Letters*, 308(3–4), 317–324.
1176 <https://dx.doi.org/10.1016/j.epsl.2011.06.003>

1177 Teng, F. Z., Dauphas, N., Huang, S., & Marty, B. (2013). Iron isotopic systematics of
1178 oceanic basalts. *Geochimica et Cosmochimica Acta*, 107, 12–26.
1179 <https://dx.doi.org/10.1016/j.gca.2012.12.027>

1180 Toutain, J. P., Sonke, J., Munoz, M., Nonell, A., Polvé, M., Viers, J., et al. (2008).
1181 Evidence for Zn isotopic fractionation at Merapi volcano. *Chemical Geology*,
1182 253(1–2), 74–82. <https://dx.doi.org/10.1016/j.chemgeo.2008.04.007>

1183 Urey, H. C. (1947). The thermodynamic properties of isotopic substances. *Journal of the*
1184 *Chemical Society (Resumed)*, 1947, 562–581.
1185 <https://dx.doi.org/10.1039/jr9470000562>

1186 Vance, D., Archer, C., Bermin, J., Perkins, J., Statham, P. J., Lohan, M. C., et al. (2008).
1187 The copper isotope geochemistry of rivers and the oceans. *Earth and Planetary*
1188 *Science Letters*, 274(1–2), 204–213. <https://dx.doi.org/10.1016/j.epsl.2008.07.026>

1189 Van Dover, C. L., Humphris, S. E., Fornari, D., Cavanaugh, C. M., Collier, R., Goffredi,
1190 S. K., et al. (2001). Biogeography and ecological setting of Indian Ocean
1191 hydrothermal vents. *Science*, 294(5543), 818–823.
1192 <https://dx.doi.org/10.1126/science.1064574>

1193 Wang, Z. Z., Liu, S. A., Liu, J., Huang, J., Xiao, Y., Chu, Z. Y., et al. (2017). Zinc
1194 isotope fractionation during mantle melting and constraints on the Zn isotope
1195 composition of Earth’s upper mantle. *Geochimica et Cosmochimica Acta*, 198,
1196 151–167. <https://dx.doi.org/10.1016/j.gca.2016.11.014>

1197 Weyer, S., Anbar, A. D., Brey, G. P., Münker, C., Mezger, K., & Woodland, A. B. (2005).
1198 Iron isotope fractionation during planetary differentiation. *Earth and Planetary*
1199 *Science Letters*, 240(2), 251–264. <https://dx.doi.org/10.1016/j.epsl.2005.09.023>
1200 Weyer, S., & Ionov, D. A. (2007). Partial melting and melt percolation in the mantle: the
1201 message from Fe isotopes. *Earth and Planetary Science Letters*, 259(1–2),
1202 119–133. <https://dx.doi.org/10.1016/j.epsl.2007.04.033>
1203 Weyer, S., & Seitz, H. M. (2012). Coupled lithium- and iron isotope fractionation during
1204 magmatic differentiation. *Chemical Geology*, 294–295, 42–50.
1205 <https://dx.doi.org/10.1016/j.chemgeo.2011.11.020>
1206 Wilkinson, J. J., Weiss, D. J., Mason, T. F. D., & Coles, B. J. (2005). Zinc isotope
1207 variation in hydrothermal systems: preliminary evidence from the Irish Midlands
1208 ore field. *Economic Geology*, 100(3), 583–590.
1209 <https://dx.doi.org/10.2113/gsecongeo.100.3.583>
1210 Williams, H. M., & Bizimis, M. (2014). Iron isotope tracing of mantle heterogeneity
1211 within the source regions of oceanic basalts. *Earth and Planetary Science Letters*,
1212 404, 396–407. <https://dx.doi.org/10.1016/j.epsl.2014.07.033>
1213 Williams, H. M., Nielsen, S. G., Renac, C., Griffin, W. L., O'Reilly, S. Y., McCammon,
1214 C. A., et al. (2009). Fractionation of oxygen and iron isotopes by partial melting
1215 processes: implications for the interpretation of stable isotope signatures in mafic

1216 rocks. *Earth and Planetary Science Letters*, 283(1–4), 156–166.

1217 <https://dx.doi.org/10.1016/j.epsl.2009.04.011>

1218 Woodhead, J. D., Eggins, S. M., & Johnson, R. W. (1998). Magma genesis in the New

1219 Britain island arc: further insights into melting and mass transfer processes.

1220 *Journal of Petrology*, 39(9), 1641–1668.

1221 <https://dx.doi.org/10.1093/petroj/39.9.1641>

1222 Woodhead, J. D., & Johnson, R. W. (1993). Isotopic and trace-element profiles across the

1223 New Britain island arc, Papua New Guinea. *Contributions to Mineralogy and*

1224 *Petrology*, 113(4), 479–491. <https://dx.doi.org/10.1007/bf00698317>

1225 Workman, R. K., & Hart, S. R. (2005). Major and trace element composition of the

1226 depleted MORB mantle (DMM). *Earth and Planetary Science Letters*, 231(1–2),

1227 53–72. <https://dx.doi.org/10.1016/j.epsl.2004.12.005>

1228 Workman, R. K., Hart, S. R., Jackson, M., Regelous, M., Farley, K. A., Blusztajn, J., et al.

1229 (2004). Recycled metasomatized lithosphere as the origin of the Enriched Mantle

1230 II (EM2) end-member: evidence from the Samoan volcanic chain. *Geochemistry,*

1231 *Geophysics, Geosystems*, 5(4), Q04008. <https://dx.doi.org/10.1029/2003gc000623>

1232 Wu, J., & Boyle, E. A. (1997). Low blank preconcentration technique for the

1233 determination of lead, copper, and cadmium in small-volume seawater samples by

1234 isotope dilution ICPMS. *Analytical Chemistry*, 69(13), 2464–2470.

1235 <https://dx.doi.org/10.1021/ac961204u>

1236 Yamaoka, K., Hong, E., Ishikawa, T., Gamo, T., & Kawahata, H. (2015). Boron isotope
1237 geochemistry of vent fluids from arc/back-arc seafloor hydrothermal systems in
1238 the western Pacific. *Chemical Geology*, 392, 9–18.
1239 <https://dx.doi.org/10.1016/j.chemgeo.2014.11.009>

1240 Zeng, Z., Chen, D., Yin, X., Wang, X., Zhang, G., & Wang, X. (2010). Elemental and
1241 isotopic compositions of the hydrothermal sulfide on the East Pacific Rise near
1242 13°N. *Science China Earth Sciences*, 53(2), 253–266.
1243 <https://dx.doi.org/10.1007/s11430-010-0013-3>

1244 Zeng, Z., Chen, S., Selby, D., Yin, X., & Wang, X. (2014). Rhenium–osmium abundance
1245 and isotopic compositions of massive sulfides from modern deep-sea
1246 hydrothermal systems: implications for vent associated ore forming processes.
1247 *Earth and Planetary Science Letters*, 396, 223–234.
1248 <https://dx.doi.org/10.1016/j.epsl.2014.04.017>

1249 Zeng, Z., Ma, Y., Chen, S., Selby, D., Wang, X., & Yin, X. (2017). Sulfur and lead
1250 isotopic compositions of massive sulfides from deep-sea hydrothermal systems:
1251 implications for ore genesis and fluid circulation. *Ore Geology Reviews*, 87,
1252 155–171. <https://dx.doi.org/10.1016/j.oregeorev.2016.10.014>

1253 Zeng, Z., Ma, Y., Yin, X., Selby, D., Kong, F., & Chen, S. (2015). Factors affecting the
1254 rare earth element compositions in massive sulfides from deep-sea hydrothermal

1255 systems. *Geochemistry, Geophysics, Geosystems*, 16(8), 2679–2693.

1256 <https://dx.doi.org/10.1002/2015gc005812>

1257 Zeng, Z., Niedermann, S., Chen, S., Wang, X., & Li, Z. (2015). Noble gases in sulfide

1258 deposits of modern deep-sea hydrothermal systems: implications for heat fluxes

1259 and hydrothermal fluid processes. *Chemical Geology*, 409, 1–11.

1260 <https://dx.doi.org/10.1016/j.chemgeo.2015.05.007>

1261 Zhao, X., Zhang, H., Zhu, X., Tang, S., & Yan, B. (2012). Iron isotope evidence for

1262 multistage melt–peridotite interactions in the lithospheric mantle of eastern China.

1263 *Chemical Geology*, 292–293, 127–139.

1264 <https://dx.doi.org/10.1016/j.chemgeo.2011.11.016>

1265 Zhao, X., Zhang, H., Zhu, X., Zhu, B., & Cao, H. (2015). Effects of melt percolation on

1266 iron isotopic variation in peridotites from Yangyuan, North China Craton.

1267 *Chemical Geology*, 401, 96–110.

1268 <https://dx.doi.org/10.1016/j.chemgeo.2015.02.031>

1269 Zhao, Y., Vance, D., Abouchami, W., & de Baar, H. J. W. (2014). Biogeochemical

1270 cycling of zinc and its isotopes in the Southern Ocean. *Geochimica et*

1271 *Cosmochimica Acta*, 125, 653–672. <https://dx.doi.org/10.1016/j.gca.2013.07.045>

1272 Zheng, J. P., Zhang, R. Y., Griffin, W. L., Liou, J. G., & O'Reilly, S. Y. (2005).

1273 Heterogeneous and metasomatized mantle recorded by trace elements in minerals

1274 of the Donghai garnet peridotites, Sulu UHP terrane, China. *Chemical Geology*,
1275 221(3–4), 243–259. <https://dx.doi.org/10.1016/j.chemgeo.2005.05.002>

1276 Zhou, J. X., Huang, Z. L., Zhou, M. F., Zhu, X. K., & Muchez, P. (2014). Zinc, sulfur
1277 and lead isotopic variations in carbonate-hosted Pb–Zn sulfide deposits, southwest
1278 China. *Ore Geology Reviews*, 58, 41–54.
1279 <https://dx.doi.org/10.1016/j.oregeorev.2013.10.009>

1280 Zhu, X. K., O'Nions, R. K., Guo, Y., Belshaw, N. S., & Rickard, D. (2000). Determination
1281 of natural Cu-isotope variation by plasma-source mass spectrometry: implications
1282 for use as geochemical tracers. *Chemical Geology*, 163(1–4), 139–149.
1283 [https://dx.doi.org/10.1016/s0009-2541\(99\)00076-5](https://dx.doi.org/10.1016/s0009-2541(99)00076-5)

1284

1285

1286

1287

1288

1289

1290

1291

1292

1293

1294 **Figure Captions**

1295 **Figure 1.** Locations of the seafloor mid-ocean ridge sulfide (MORS), BAB sulfide
1296 (BABS), and their host mid-ocean ridge basalt (MORB) samples from deep-sea
1297 hydrothermal fields analyzed for Fe, Cu, and Zn isotopic compositions. EHF: Edmond
1298 hydrothermal field; CIR: Central Indian Ridge; SWIR: Southwest Indian Ridge; S99HF:
1299 Sonne 99 hydrothermal field; NFB: North Fiji back-arc basin; EPR: East Pacific Rise.

1300 **Figure 2.** $\delta^{56}\text{Fe}$ values of the mid-ocean ridge basalt (MORB), mid-ocean ridge sulfide
1301 (MORS), and back-arc basin sulfides (BABS) samples. The $\delta^{56}\text{Fe}$ ranges of previously
1302 studied MORBs (Teng et al., 2013), ocean island basalts (OIBs) (Beard, Johnson, Skulan,
1303 et al., 2003; Teng et al., 2013), seawater (Rouxel & Auro, 2010), sediments (Rouxel et al.,
1304 2003; Severmann et al., 2004), and hydrothermal fluids (Moeller et al., 2014; Rouxel et
1305 al., 2008; Severmann et al., 2004; Sharma et al., 2001), basalts from the North Fiji
1306 back-arc basin (Teng et al., 2013), and MORS minerals from the EPR between 9° and
1307 10°N (Rouxel et al., 2008) and the JdFR (Sharma et al., 2001) are also illustrated. Py:
1308 pyrite; Cpy: chalcopyrite; Sp: sphalerite.

1309 **Figure 3.** $\delta^{65}\text{Cu}$ values of the mid-ocean ridge basalt (MORB), mid-ocean ridge sulfide
1310 (MORS), and back-arc basin sulfides (BABS) samples. The $\delta^{65}\text{Cu}$ value ranges of
1311 previously studied MORBs (Liu et al., 2015; Savage et al., 2015), ocean island basalts

1312 (OIBs) (Liu et al., 2015; Savage et al., 2015), seawater (Little et al., 2014; Vance et al.,
1313 2008), sediments (Maréchal et al., 1999), and hydrothermal fluids (Dekov & Rouxel,
1314 2012) are also presented.

1315 **Figure 4.** $\delta^{66}\text{Zn}$ values of the mid-ocean ridge basalt (MORB), mid-ocean ridge sulfide
1316 (MORS), and back-arc basin sulfides (BABS) samples. The $\delta^{66}\text{Zn}$ value ranges of
1317 previously studied MORBs (Ben Othman et al., 2006; Wang et al., 2017), ocean island
1318 basalts (OIBs) (Wang et al., 2017), seawater (Little et al., 2014; Samanta et al., 2017; Y.
1319 Zhao et al., 2014), sediments (Maréchal et al., 1999; Pichat et al., 2003), and
1320 hydrothermal fluids (John et al., 2008) are also shown.

1321 **Figure 5.** Plots of mid-ocean ridge (MOR) spreading rate vs. (a) $\delta^{56}\text{Fe}$, (b) $\delta^{65}\text{Cu}$, and (c)
1322 $\delta^{66}\text{Zn}$ for the mid-ocean ridge basalts (MORBs) reported in this study.

1323 **Figure 6.** Plots of hydrothermal fluid temperature vs. (a) $\delta^{56}\text{Fe}$ of sulfides, (b) $\delta^{65}\text{Cu}$ of
1324 chalcopryrite, and (c) $\delta^{66}\text{Zn}$ of sphalerite from seafloor hydrothermal fields. The
1325 temperature data for the hydrothermal fluids are from Bowers et al. (1988), Grimaud et al.
1326 (1991), Ishibashi, Grimaud, et al. (1994), Ishibashi, Wakita, et al. (1994), Oosting and
1327 Von Damm (1996), Gallant and Von Damm (2006), Foustoukos and Seyfried (2007),
1328 John et al. (2008), Proskurowski et al. (2008), Rouxel et al. (2008), Ji et al. (2017), and
1329 Yamaoka et al. (2015).

1330 **Table Headings**

1331 **Table 1.** Fe-Cu-Zn isotopic compositions of the mid-ocean ridge basalts (MORBs) and
1332 reference materials.

1333 **Table 2.** Fe-Cu-Zn isotopic compositions of seafloor hydrothermal sulfides from
1334 mid-ocean ridge basalts (MORBs), back-arc basin basalt (BABBs), and reference
1335 materials.

1336

1337

1338 **SUPPORTING INFORMATION (SI)**

1339 The supporting information (SI) includes Figures. S1–S3 and Tables S1–S6.

1340

1341

1342

Figure 1.

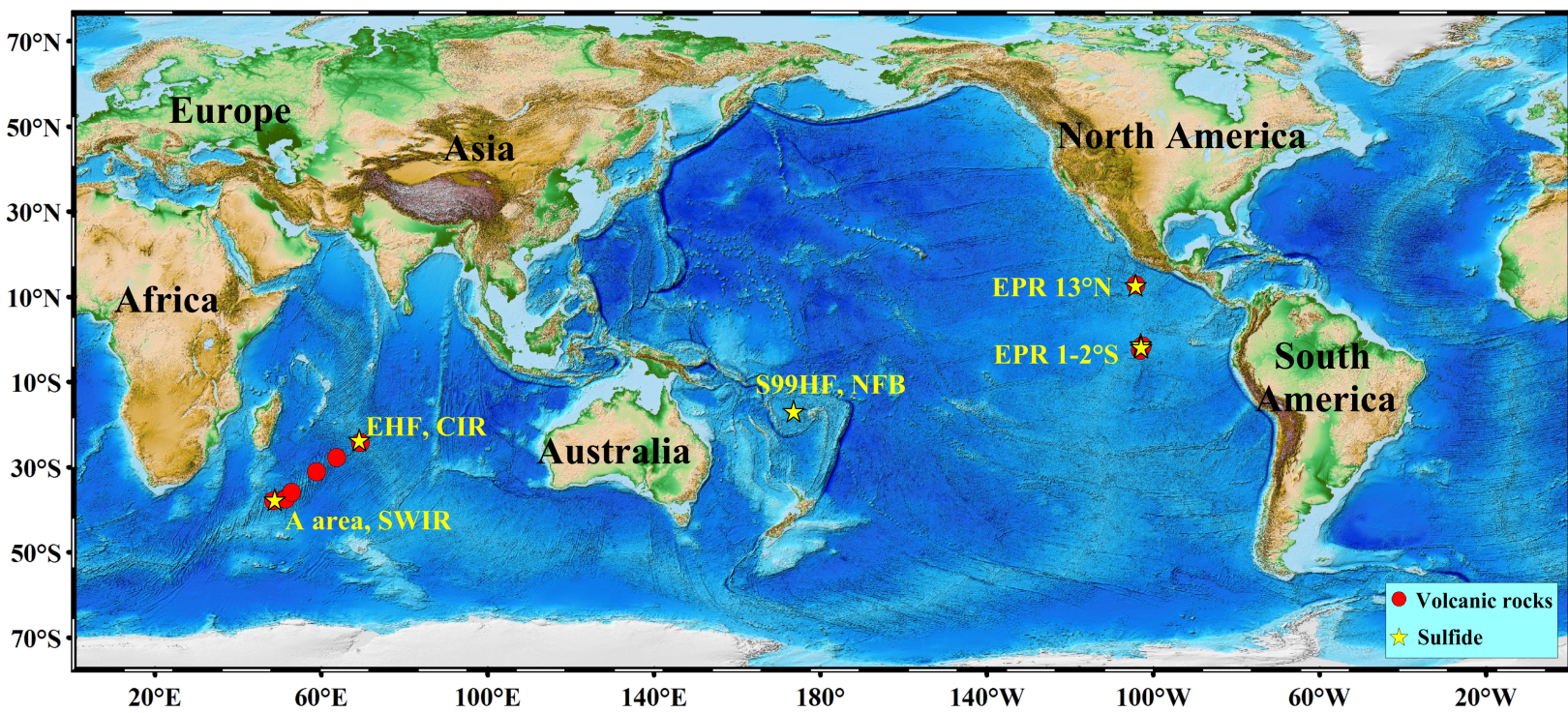


Figure 2.

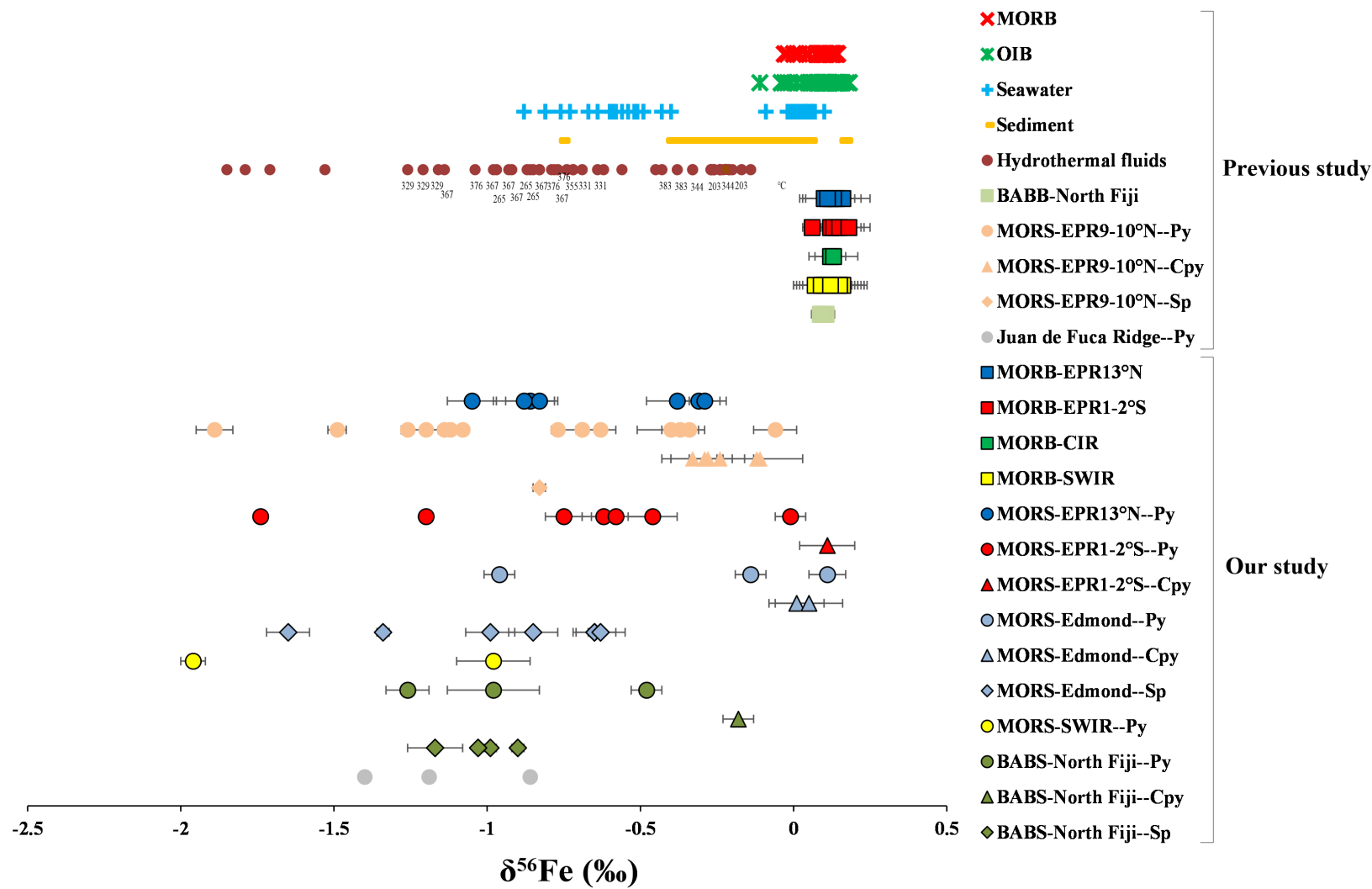


Figure 3.

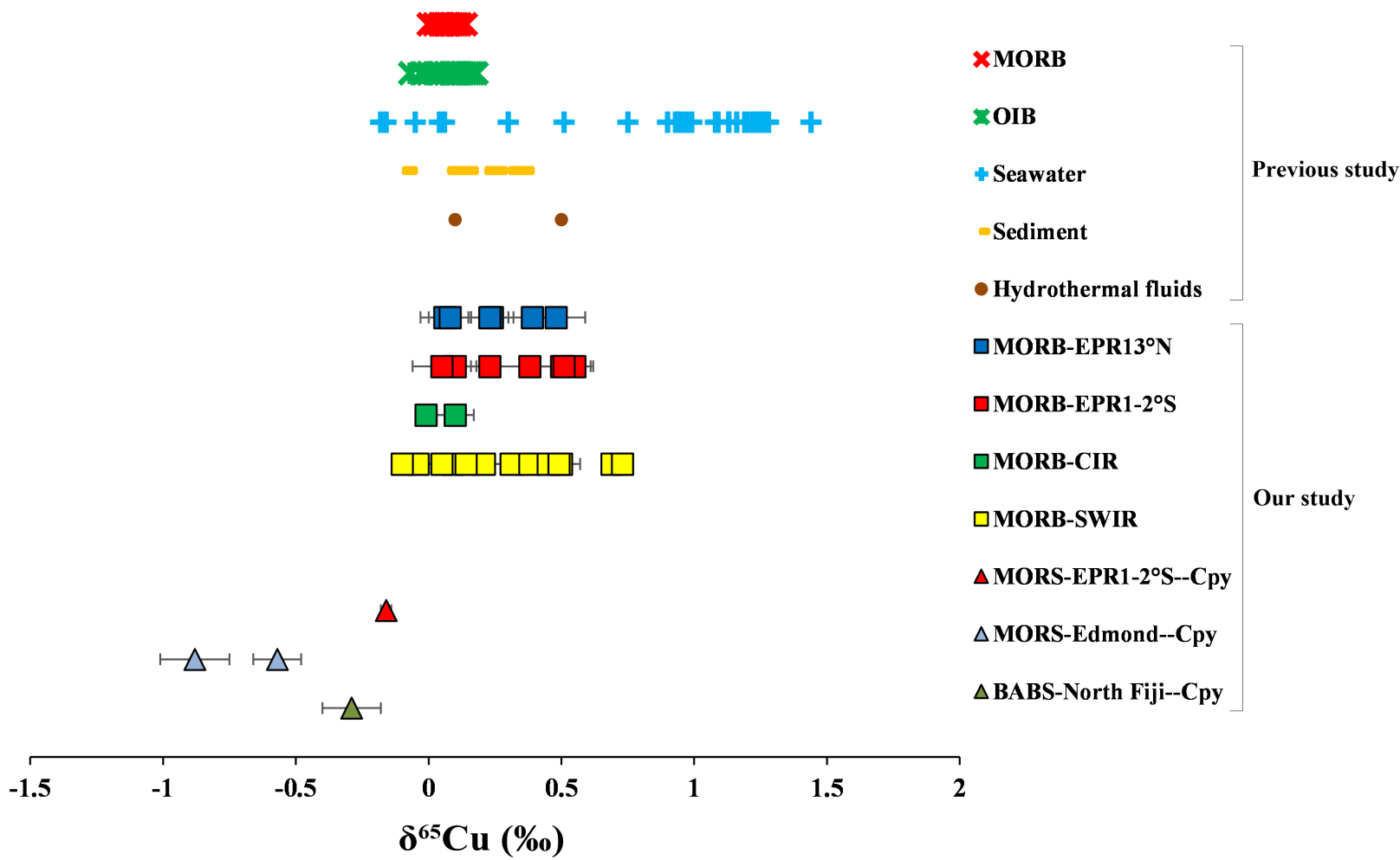


Figure 4.

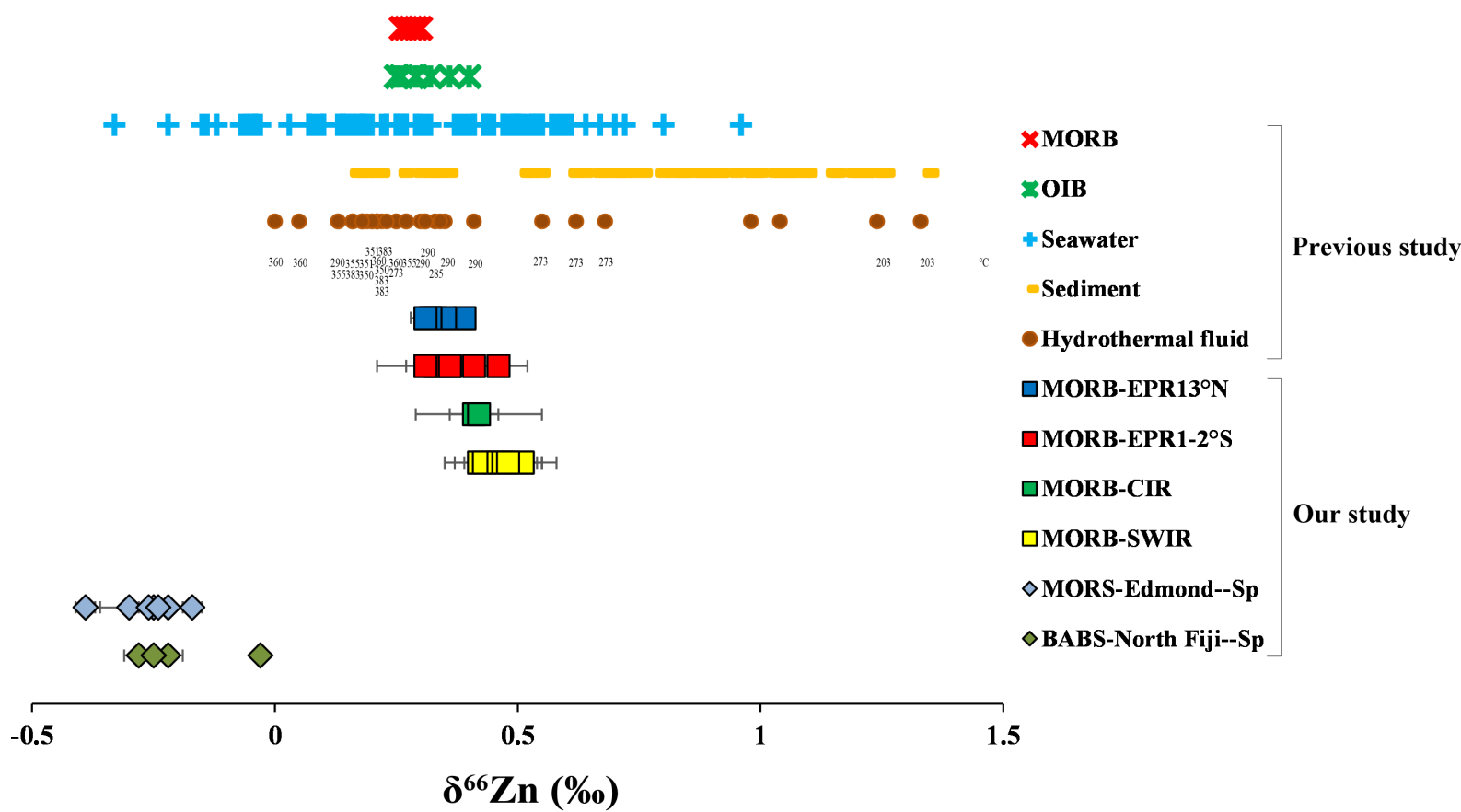


Figure 5.

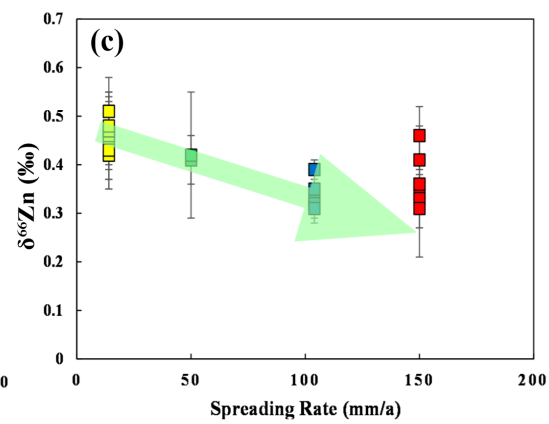
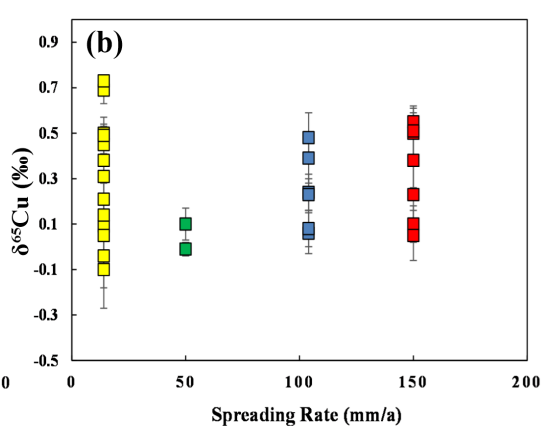
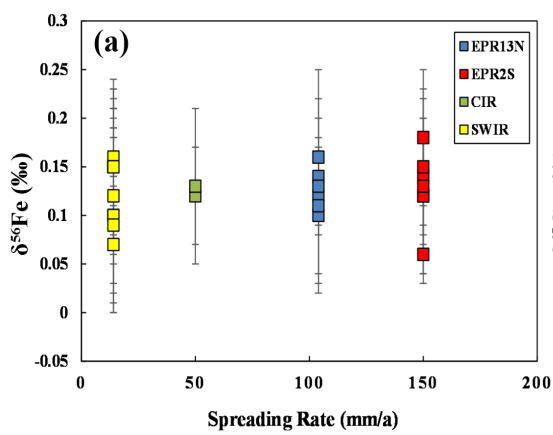


Figure 6.

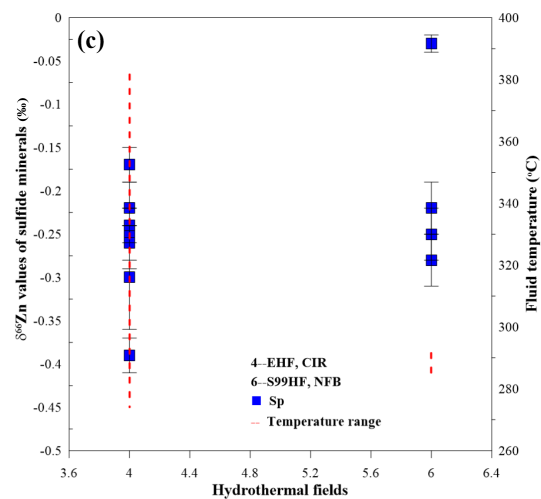
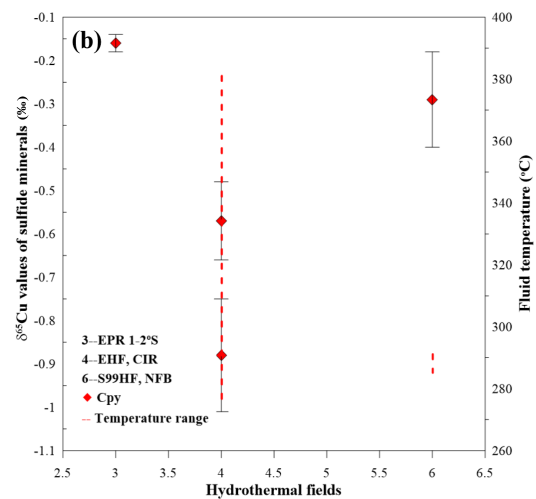
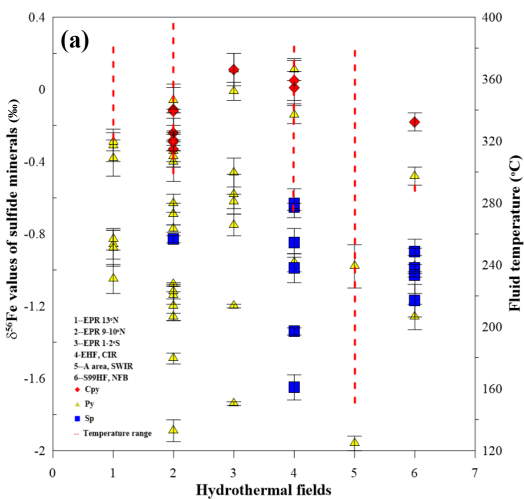


Table 1. Fe-Cu-Zn isotopic compositions of the mid-ocean ridge basalts (MORBs) and reference materials.

Sample Name	Type	Location	$\delta^{56}\text{Fe}$	2SD	$\delta^{57}\text{Fe}$	2SD	N	$\delta^{65}\text{Cu}$	2SD	N	$\delta^{68}\text{Zn}$	2SD	$\delta^{66}\text{Zn}$	2SD	N
E27-1	basalt	EPR13°N	0.10	0.08	0.12	0.10	6	0.24	0.08	3	0.67	0.04	0.33	0.01	3
E29-1	basalt	EPR13°N	0.14	0.11	0.17	0.09	3	0.23	0.07	3	0.77	0.10	0.39	0.02	3
E33-1	basalt	EPR13°N	0.12	0.08	0.14	0.09	4	0.06	0.09	3	0.67	0.08	0.32	0.02	3
E44-1	basalt	EPR13°N	0.16	0.06	0.20	0.06	3	0.08	0.08	3	0.73	0.09	0.35	0.03	3
E44-1*	basalt	EPR13°N	0.13	0.04	0.16	0.06	4	0.48	0.11	3	0.67	0.04	0.32	0.03	3
E46	basalt	EPR13°N	0.11	0.03	0.15	0.03	3	0.39	0.11	3	0.63	0.14	0.31	0.03	3
EPR05-TVG4	basalt	EPR1-2°S	0.12	0.06	0.16	0.05	3	0.23	0.13	3	0.69	0.13	0.34	0.02	3
20III-S4-TVG1	basalt	EPR1-2°S	0.14	0.06	0.15	0.08	3	0.38	0.12	3	0.65	0.19	0.33	0.06	3
20III-S8-TVG5-1	basalt	EPR1-2°S	0.12	0.08	0.15	0.11	4	0.50	0.11	3	0.62	0.19	0.31	0.10	3
20III-S10-TVG7	basalt	EPR1-2°S	0.13	0.09	0.21	0.05	3	0.55	0.04	3	0.84	0.14	0.41	0.07	6
20III-S10-TVG7*	basalt	EPR1-2°S	0.15	0.08	0.23	0.13	3	0.10	0.08	3	0.98	0.19	0.46	0.06	3
20III-S11-TVG8-1	basalt	EPR1-2°S	0.18	0.07	0.20	0.12	3	0.05	0.11	3	0.75	0.07	0.36	0.09	3
21III-S18-TVG14	basalt	EPR1-2°S	0.06	0.03	0.13	0.09	5	0.51	0.11	3	0.74	0.07	0.36	0.02	3
IR05-TVG10-1	basalt	EHF, CIR	0.12	0.05	0.16	0.12	4	-0.01	0.03	3	0.83	0.13	0.41	0.05	3
IR05-TVG11-1	basalt	EHF, CIR	0.13	0.08	0.14	0.06	5	0.10	0.07	3	0.87	0.12	0.42	0.13	2
IR05-TVG1-1	basalt	A area, SWIR	0.10	0.09	0.10	0.07	6	0.31	0.10	3	0.83	0.08	0.42	0.05	3
IR05-TVG3-1	basalt	A area, SWIR	0.10	0.10	0.20	0.08	4	-0.04	0.23	3	0.97	0.10	0.47	0.07	3
IR05-TVG4-1	basalt	A area, SWIR	0.15	0.04	0.23	0.14	4	0.69	0.06	3	0.90	0.23	0.45	0.10	3
IR05-TVG4-1*	basalt	A area, SWIR	0.15	0.08	0.24	0.11	6	0.73	0.00	1	0.99	0.24	0.46	0.09	5
IR05-TVG5-1	basalt	A area, SWIR	0.15	0.09	0.23	0.12	5	0.38	0.06	3	0.96	0.14	0.46	0.07	3
20IV-S4-TVG1	basalt	A area, SWIR	0.10	0.08	0.14	0.15	6	0.50	0.07	3	0.83	0.20	0.42	0.07	3
20V-S11-TVG3	basalt	A area, SWIR	0.07	0.07	0.17	0.04	3	0.45	0.08	3	0.88	0.11	0.43	0.02	3
20V-S34-TVG16	basalt	A area, SWIR	0.09	0.04	0.15	0.05	5	0.49	0.05	3	0.99	0.13	0.46	0.05	3
20VII-S3-TVG3	basalt	A area, SWIR	0.15	0.07	0.19	0.11	3	0.21	0.07	3	1.05	0.19	0.51	0.07	3
20VII-S7-TVG5	basalt	A area, SWIR	0.16	0.02	0.22	0.08	3	0.09	0.11	3	1.06	0.02	0.51	0.00	2
20VII-S7-TVG5*	basalt	A area, SWIR	0.15	0.08	0.19	0.09	3	0.05	0.17	3	1.03	0.15	0.47	0.05	2
20VII-S15-TVG13-1	basalt	A area, SWIR	0.15	0.06	0.23	0.04	3	0.14	0.02	3	1.00	0.06	0.47	0.03	3
20VII-S20-TVG17-1	basalt	A area, SWIR	0.12	0.09	0.21	0.07	3	-0.10	0.08	3	0.99	0.08	0.48	0.07	2
<i>Reference materials</i>															
IRMM-014			0.00	0.08	0.01	0.10	43								
MIX			-1.55	0.09	-2.27	0.13	29								
Average Quality control 'Mix' on Nu Plasma I			-1.53	0.07	-2.26	0.15	6								
JMC Cu110 in-house solutions								1.06	0.16	30					
SRM NIST 976 Cu								-0.97	0.13	27					
BHVO-2								0.00	0.07	9					
JMC Zn310 in-house solutions											-0.20	0.10	-0.10	0.06	20
IRMM-3702 Zn											0.63	0.16	0.32	0.08	8

* Indicates the analysis result of a duplicate sample.

1 **Table 2.** Fe-Cu-Zn isotopic compositions of seafloor hydrothermal sulfides from mid-ocean ridge basalts (MORBs), back-arc
2 basin basalt (BABBs), and reference materials.

Sample Name	Mineral	Location	$\delta^{56}\text{Fe}$	2SD	$\delta^{57}\text{Fe}$	2SD	N	$\delta^{65}\text{Cu}$	2SD	N	$\delta^{68}\text{Zn}$	2SD	$\delta^{66}\text{Zn}$	2SD	N
<i>Mid-ocean ridge sulfides (MORS)</i>															
EPR05-TVG1-2-1	Py	EPR13°N	-0.31	0.09	-0.41	0.09	6								
EPR05-TVG1-2-1*	Py	EPR13°N	-0.29	0.05	-0.40	0.16	6								
EPR05-TVG1-2-4	Py	EPR13°N	-0.38	0.10	-0.57	0.20	6								
EPR05-TVG1-3-2	Py	EPR13°N	-0.86	0.08	-1.30	0.16	5								
EPR05-TVG1-3-3	Py	EPR13°N	-0.83	0.06	-1.26	0.07	3								
EPR05-TVG2-1-2	Py	EPR13°N	-1.05	0.08	-1.58	0.21	3								
EPR05-TVG2-1-4	Py	EPR13°N	-0.88	0.10	-1.34	0.13	5								
20III-S4-TVG1-1-1	Py	EPR1-2°S	-0.75	0.06	-1.11	0.14	3								
20III-S4-TVG1-1-2	Py	EPR1-2°S	-0.62	0.04	-0.87	0.06	3								
20III-S4-TVG1-1-3	Py	EPR1-2°S	-0.46	0.08	-0.68	0.13	3								
20III-S4-TVG1-1-4	Py	EPR1-2°S	-0.58	0.11	-0.90	0.12	3								
20III-S4-TVG1-2-3	Py	EPR1-2°S	-0.01	0.05	-0.08	0.11	3								
20III-S4-TVG1-2-3*	Py	EPR1-2°S	-1.74	0.01	-2.58	0.09	3								
20III-S6-TVG3	Py	EPR1-2°S	-1.20	0.01	-1.80	0.07	2								
20III-S4-TVG1-2-3	Cpy	EPR1-2°S	0.11	0.09	0.19	0.03	3	-0.16	0.02	3					
IR05-TVG12-11	Py	EHF, CIR	-0.14	0.05	-0.18	0.08	3								
IR05-TVG12-14	Py	EHF, CIR	0.11	0.06	0.12	0.09	3								
19III-S18-TVG9	Py	EHF, CIR	-0.96	0.05	-1.43	0.06	6								
IR05-TVG13-4-1	Cpy	EHF, CIR	0.01	0.09	0.00	0.10	3	-0.57	0.09	3					
19III-S18-TVG9	Cpy	EHF, CIR	0.05	0.11	0.07	0.16	3	-0.88	0.13	3					
IR05-TVG12-5-2	Sp	EHF, CIR	-0.65	0.02	-0.93	0.08	3				-0.35	0.03	-0.17	0.02	3
IR05-TVG12-8-2	Sp	EHF, CIR	-0.85	0.08	-1.27	0.15	4				-0.47	0.03	-0.25	0.01	3
IR05-TVG12-8-4	Sp	EHF, CIR	-0.65	0.07	-0.93	0.09	3				-0.61	0.09	-0.30	0.06	3
IR05-TVG12-8-4*	Sp	EHF, CIR	-0.99	0.08	-1.45	0.20	3				-0.77	0.03	-0.39	0.02	3
IR05-TVG12-9-1	Sp	EHF, CIR	-1.65	0.07	-2.48	0.15	4				-0.43	0.00	-0.22	0.00	3
IR05-TVG12-11	Sp	EHF, CIR	-0.63	0.08	-0.98	0.15	3				-0.49	0.07	-0.26	0.02	3
IR05-TVG13-9.2-1	Sp	EHF, CIR	-1.34	0.02	-1.97	0.06	3				-0.45	0.11	-0.24	0.05	3
19II-S7-TVG4	Py	A area, SWIR	-1.96	0.04	-2.89	0.07	6								
21VII-TVG22	Py	A area, SWIR	-0.98	0.12	-1.47	0.06	4								
<i>Back-arc basin sulfides (BABS)</i>															
113.1GTV-1	Py	NFB	-0.98	0.15	-1.44	0.08	6								
113.1GTV-4	Py	NFB	-0.48	0.05	-0.73	0.06	3								
113.2GTV	Py	NFB	-1.26	0.07	-1.81	0.04	3								
113.1GTV-4	Cpy	NFB	-0.18	0.05	-0.25	0.10	3	-0.29	0.11	3					
26.1GTV-1	Sp	NFB	-0.99	0.02	-1.46	0.10	3				-0.44	0.05	-0.22	0.03	3
26.1GTV-2	Sp	NFB	-1.03	0.01	-1.50	0.10	3				-0.55	0.05	-0.28	0.03	3
26.2GTV-1	Sp	NFB	-0.90	0.02	-1.34	0.04	3				-0.03	0.07	-0.03	0.01	3
26.2GTV-3	Sp	NFB	-1.17	0.09	-1.77	0.17	3				-0.51	0.04	-0.25	0.03	3
<i>Reference materials</i>															
IRMM-014			0.00	0.03	0.01	0.08	25								
MIX			-1.55	0.12	-2.25	0.17	32								
Average Quality control 'Mix' on Nu Plasma I			-1.53	0.07	-2.26	0.15	6								
JMC Cu110 in-house solutions								1.06	0.16	30					
SRM NIST 976 Cu								-0.97	0.13	27					
BHVO-2								0.00	0.07	9					
JMC Zn310 in-house solutions											-0.20	0.09	-0.10	0.03	11
IRMM 3702 Zn											0.59	0.04	0.28	0.01	3
Lyon JMC 3-0749L Zn											0.00	0.03	0.00	0.04	3

* Indicates the analysis result of a duplicate sample.